FILTERING OF ACOUSTIC INFORMATION FROM AERO-OPTICAL MEASUREMENTS

A Dissertation

Submitted to the Graduate School

of the University of Notre Dame

in Partial Fulfillment of the Requirements

for the Degree of

Doctor of Philosophy

by

Brian Lowell Catron

R. Mark Rennie , Co-Director

Eric J. Jumper, Co-Director

Graduate Program in Aerospace and Mechanical Engineering

Notre Dame, Indiana

December 2021

FILTERING OF ACOUSTIC INFORMATION FROM AERO-OPTICAL MEASUREMENTS

Abstract

by

Brian Lowell Catron

Abstract Goes Here

To my wife Karen & our son Arthur

CONTENTS

FIGURES

TABLES

SYMBOLS

Ap	Aperture size - Typically diameter
I	Actual on target intensity
I_0	Diffraction-limited intensity
k	Wavenumber ($k = 2\pi/\lambda$)
n	Index of refraction
OPD	Optical path difference
$\mathrm{OPD}_{\mathrm{RMS}}$	Spatial OPD root-mean-square
SR	Strehl ratio ($\mathrm{SR} = I/I_0$)
	Greek
δ	Boundary layer thickness
$\langle\theta^2\rangle$	Mean-squared of the fluctuating deflection angle

ACKNOWLEDGMENTS

CHAPTER 1

INTRODUCTION

Directed-energy systems have a variety of uses but typically fall into one of two categories: communications and weapons. The primary benefits of directed-energy communications is the ability to have secure point-to-point data transfer that is high unlikely to intercept or be interfered with [34]. Directed-energy weapons are likely to have a lower cost per shot and a deeper magazine when compared to traditional munitions [35]. As ground based directed-energy systems are slowly rolled out, most prominently aboard the USS Ponce [33], there is a desire to field a system aboard an aircraft.

There have been two major attempts to field a directed-energy system aboard an aircraft to date [18]. The first was the Airborne Laser Laboratory (ALL) which took place in the late 1970's and early 1980's which used a CO_2 laser at 10.6-μm. The second was the Airborne Laser (ABL) program which operated in the 2000's and used a COIL laser at 1.315-μm. Airborne optical systems have to deal with a phenomenon know as "aero-optics," which is optical distortions caused by various aero-dynamic flow features. These optical distortions were first noticed due to image degradation in wind tunnel measurements in the 1950's [39] as well as in photo-reconnaissance missions in the 1960's [20].

The intensity of that makes through an optical disturbance to a target, I, divided by the diffraction-limited performance, I_0, is known as the Strehl ratio [23], SR,

$$\mathrm{SR} = \frac{I}{I_0}. \tag{1.1}$$

The diffraction-limited performance is the intensity that would make it to the same target if not for a disturbance. The Airborne Laser Laboratory had an estimated Strehl ratio of 95%[18] meaning the "aero-optics problem" effectively did not apply. After the Airborne Laser Laboratory program there was a desire to move toward shorter wavelengths in order to take advantage of improved

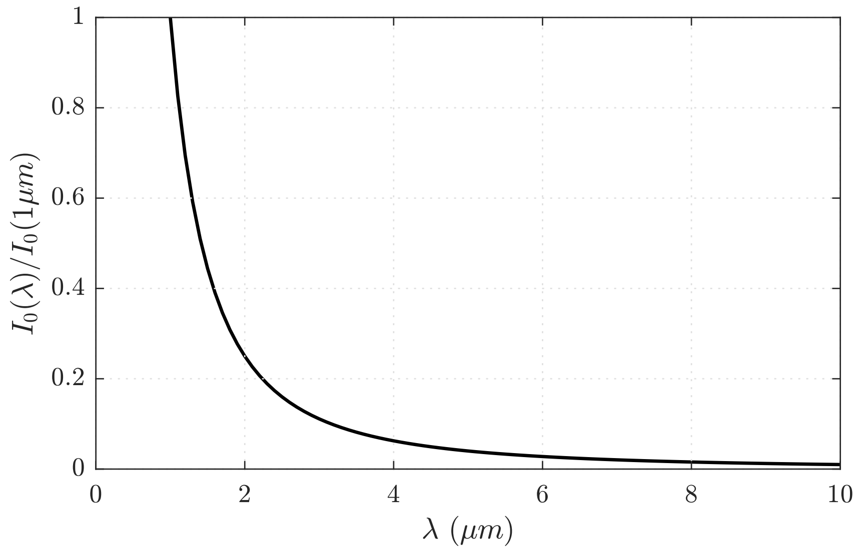

Figure 1.1. Diffraction-limited far-field intensity of a beam normalized by the performance at 1-μm.

diffraction-limited performance [17],

$$\frac{I_0}{P} = \frac{1}{\pi}\left(\frac{Ap}{\lambda z}\right)^2, \tag{1.2}$$

where P is the laser output power, Ap is the aperture size, and z is the propagation distance. This improved diffraction-limited performance is shown in Figure 1.1. By only changing the laser source from a 10-μm to 1-μm wavelength the diffraction-limited performance can be increased 100 times.

Aero-optical issues start to become apparent as the wavelength is decreased as is evident by the Maréchal approximation [24] which relates the Strehl ratio to wavelength,

$$\mathrm{SR} \approx \exp\left\{-\left[\frac{2\pi\,\mathrm{OPD_{RMS}}}{\lambda}\right]^2\right\}, \tag{1.3}$$

where $\mathrm{OPD_{RMS}}$ is the spatial root-mean-square of the optical path difference over the aperture and is a way to quantify the optical disturbance that will be discussed in Chapter 2. If the ALL system's laser was swapped with another laser of a lower wavelength, the Strehl ratio would significantly decrease as shown by Figure 1.2. While the hypothetical case of going from 10 to 1-μm resulted in a 100-fold increase in diffraction-limited performance, the actual on-target intensity that this hypothetical system obtains would be essentially zero. This means that the aero-optical problem

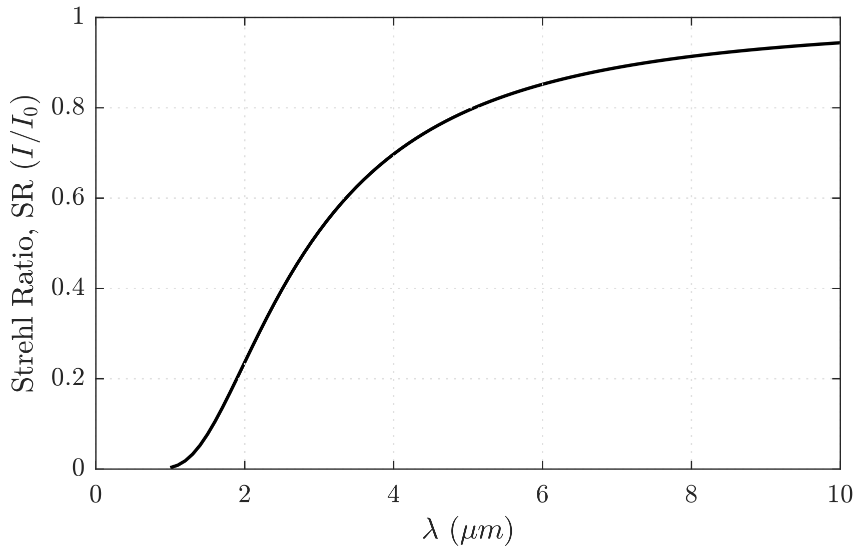

Figure 1.2. Strehl ratio due to the $\mathrm{OPD_{RMS}}$ of the Airborne Laser Laboratory (ALL) at various laser wavelengths. ALL had an estimated Strehl ratio of 95% with its 10.6-μm laser.

can no longer be ignored and was recognized as one of the main developmental risks of the ABL program [10]. Do you have or know of a source that at the very least alludes to the aero-optical issues with ABL that greatly limited its field of regard?

As the next generation of airborne directed-energy systems are developed some amount of ground testing of those systems will need to occur. In order to understand the aero-optical environment that these systems will experience in the air wind tunnel tests will need to be employed. These tests are far cheaper to perform and allow for quicker iteration of design parameters. Wind tunnel tests will however include some additional optical contamination including but not limited to the boundary layer present on the wall and the acoustic environment generated by the wind tunnel fan [14]. Assuming that the optical disturbances system model are statistically independent from the optical disturbances from the testing environment, we can estimate the total optical disturbance from

$$\mathrm{OPD_{RMS}}^2_{TOTAL} = \mathrm{OPD_{RMS}}^2_{MODEL} + \mathrm{OPD_{RMS}}^2_{ENVIRONMENT} \,. \tag{1.4}$$

This combination of optical disturbances is shown in Figure 1.3 along with a hypothetical iterative design process. This process seeks to obtain a design that meets a required level of performance shown in red. If only the measured data is used to assess the system's performance three additional iterative changes are needed to achieve a usable design which can add significantly

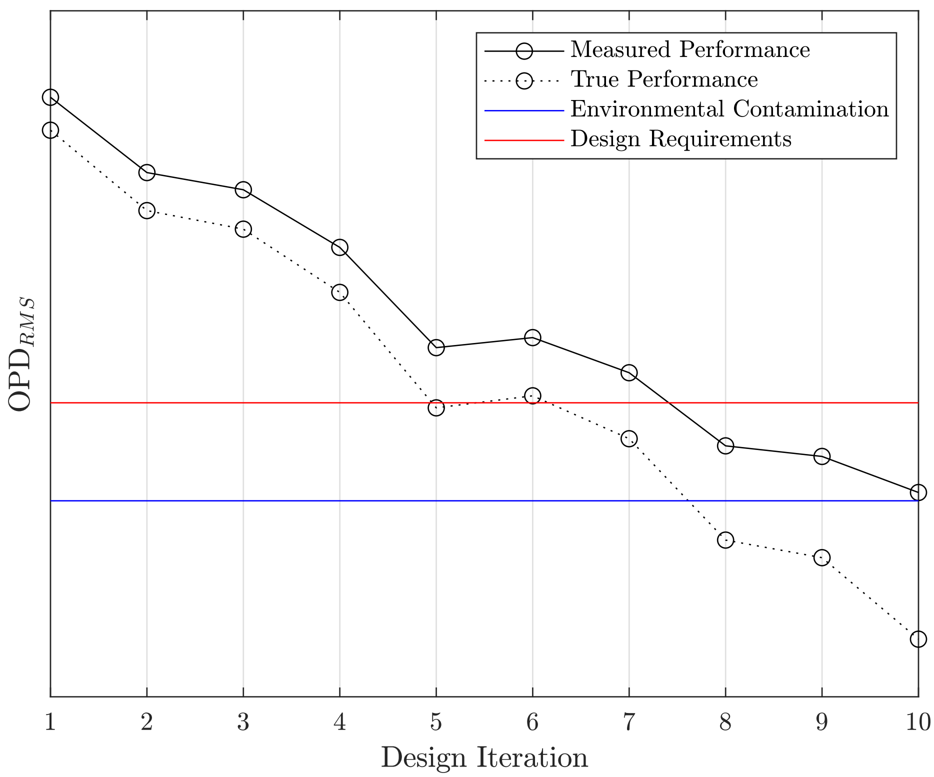

Figure 1.3. Hypothetical iterative design process of an airborne directed-energy system. The required performance level is shown by the red line and the testing environment's contamination is shown by the blue line.

to the development time and costs. If the environmental contamination is greater than the design requirement, the measured performance will never reach the required performance criteria. When the true performance of a system is significantly higher than the environmental contamination, the measured performance is not significantly greater than the true performance. The measured performance becomes significantly greater that the true performance when the true performance is less than the environmental contamination.

This dissertation will primary examine the environmental contamination due to acoustic noise within the wind tunnel. In Chapter 3 it will look at the optical disturbances caused by acoustic waves from some simple plane and spherical waves to a process for estimating the acoustic environment within the test section of a wind tunnel. The strength of an spherical acoustic wave will be assessed with both microphone and optical measurements. Multi-dimensional spectral techniques will be used to analyze optical wavefronts in Chapter 4 and filter optical wavefronts in Chapter 6. These filtering techniques will contain some optical contamination particularly in regions where the various signal components interfere with one another. In order to further reduce the optical contamination, Chapter 7 will utilize additional sensor information from both microphones and accelerators to remove some of the overlapping contamination to obtain a better picture of the actual optical performance of an airborne directed-energy system from ground test measurements.

CHAPTER 2

LITERATURE REVIEW

The literature review will consist of primarily two sections. The first section will examine aero-optics while the second will look at acoustics inside of ducts.

2.1 Aero-Optics

Optical communication and directed energy systems require a tightly focused beam on target in order to meet system performance objectives. The farfield performance of airborne optical systems can be degraded by the nearfield flow that becomes optically active at compressible flow speeds. "Aero-optics" is the study of the optical effect of these nearfield flow disturbances. Examples of important aero-optical flows that have been studied extensively include boundary layers [14, 38, 41], shear layers [11, 31], shock waves [18], and even tip vortices [29]. The effect of acoustic disturbances on aero-optical measurements has also been shown in both flight testing [9] and ground testing [6, 7].

In these optically active flows the index-of-refraction, n, varies locally as does the other fluid properties. Gladstone and Dale [12] found that the index-of-refraction is primarily a function of density with a loose dependence on the wavelength of light. Gladstone and Dale proposed a "specific refractive energy" now known as the Gladstone-Dale constant, K_{GD},

$$K_{GD} = \frac{n-1}{\rho}. \tag{2.1}$$

For air the refractive index can be related to state quantities [40]

$$n - 1 = 77.6 \times 10^{-6} \frac{P}{T} \left(1 + \frac{7.53 \times 10^{-3}}{\lambda^2}\right), \tag{2.2}$$

where P is in mbar, T is in K, and λ is in μm. By combining this relationship with the ideal gas law, the Gladstone-Dale constant can be determined as a function of light wavelength,

$$K_{GD} = 2.23 \times 10^{-4} \left(1 + \frac{7.53 \times 10^{-3}}{\lambda_{\mu m}^2}\right) \left[\frac{m^3}{kg}\right]. \tag{2.3}$$

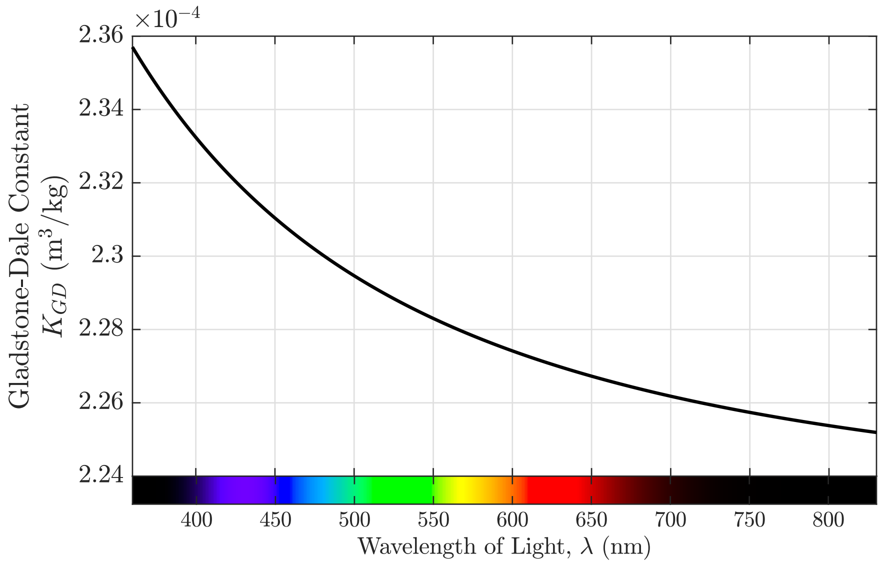

Figure 2.1. Gladstone-Dale constant for air over the visible wavelength range.

The Gladstone-Dale constant for air over the visible range is shown in Figure 2.1. While the value for K_{GD} does vary over the visible range, it is only a few percent, and many sources use an average value of 2.27×10^{-4} m^3/kg for the visible and near-infrared [16]. The Gladstone-Dale relationship is typically presented as

$$n = 1 + K_{GD}\rho \tag{2.4}$$

but when applied to situations where there are significant fluctuations in the flow an alternate form is often more useful

$$n' = K_{GD}\rho' \tag{2.5}$$

where $'$ denotes the quantity represents the fluctuating component ($n' = n - \bar{n}$).

When a beam with an initially planar wave front passes through a region of optical active flow its wave front aberrated The optical path length (OPL) at any point in the beam can be obtained by integrating the index of refraction along the propagation of an optical ray [19].

$$\mathrm{OPL}(x, y, t) = \int_{s_1}^{s_2} n(x, y, z, t)ds \tag{2.6}$$

The optical path difference (OPD), is then the spatially-averaged OPL over an aperture removed from the OPL.

$$\mathrm{OPD}(x, y, t) = \mathrm{OPL}(x, y, t) - \langle \mathrm{OPL}(x, y, t)\rangle \tag{2.7}$$

When working with fluctuating components, the OPD can be calculated directly

$$\mathrm{OPD}(x,y,t) = \int_{s_1}^{s_2} n'(x,y,z,t)ds. \tag{2.8}$$

When OPD is combined with the beam intensity profile, one can compute the farfield complex amplitude distribution using the Fraunhofer approximation [13].

$$U(x_0,y_0,t) \propto \iint_{Ap} \exp\left\{\frac{2\pi j}{\lambda}\left[\mathrm{OPD}(x_1,y_1,t) - \frac{(x_0x_1+y_0y_1)}{z}\right]\right\} dx_1dy_1 \tag{2.9}$$

where U is the complex amplitude, the subscripts 0 and 1 represent the coordinates of the farfield and nearfield respectively. The intensity can be computed from the complex amplitude via: $I = UU^*$. For cases in which optical aberrations are nonexistent (i.e. $\mathrm{OPD}(x,y,t) = 0$), the farfield irradiance pattern that results from Equation 2.9 is caused entirely by diffraction from the optical aperture, and is referred to as the "diffraction-limited" irradiance pattern. For a beam with a flat wave front and circular aperture, the farfield irradiance pattern is the Airy's disk, and the peak irradiance at the center of the disk, I_0 , is the maximum irradiance that can be achieved by the optical system:

$$I_0 = \left(\frac{kAp^2}{8z}\right)^2 \tag{2.10}$$

where k is the wavenumber ($k = 2\pi/\lambda$), Ap is the aperture diameter, and z is the distance from the aperture. In the presence of aero-optical aberrations, $\mathrm{OPD}(x,y,t)$ is non-zero, and the farfield irradiance pattern in this case tends to be more spread out and diffuse than the diffraction-limited case; furthermore, the beam may be shifted off target by optical tip/tilt imposed by the aberrations.

The Strehl ratio (SR), is the ratio of intensity on target (I) to the diffraction-limited on target intensity (I_0):

$$\mathrm{SR} = \frac{I}{I_0} \tag{2.11}$$

The Strehl ratio can be computed accurately by applying Equation 2.9 twice, once for the diffraction-limited case to obtain I_0, and a second time with the OPD field due to aero-optical aberrations included to obtain I. The farfield performance, can also be estimated via the Maréchal approximation:

$$\mathrm{SR}(t) \equiv \frac{I(t)}{I_0} \approx \exp\left\{-\left[\frac{2\pi\,\mathrm{OPD_{RMS}}(t)}{\lambda}\right]^2\right\} \tag{2.12}$$

where $\mathrm{OPD_{RMS}}$ is the spatial rms of the wave front and λ is the wavelength of the beam. Equation

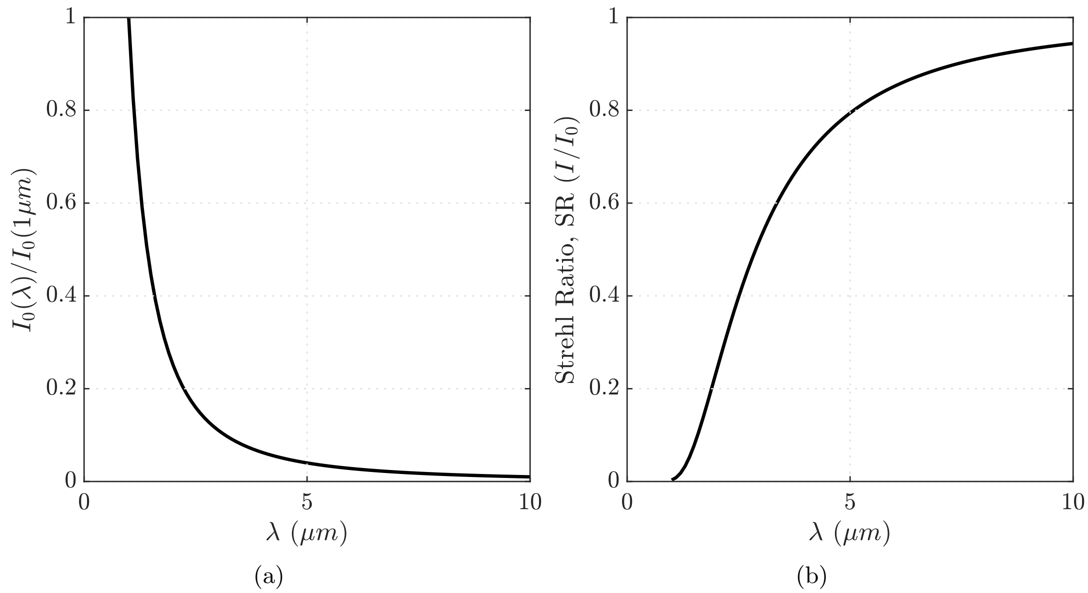

Figure 2.2. (a) Diffraction limited on target intensity as a function of wavelength normalized by the value at $\lambda = 1$ μ m. (b) Strehl ratio as a function of wavelength for an aberration that gives SR = 0.95 at $\lambda = 10.6$ μm.

2.12 shows a key relationship between OPD, wavelength, and the farfield performance, plotted in Figure 2.2b. On the other hand, Equation 2.10 shows that the diffraction-limited farfield irradiance increases as the wavelength is shortened, plotted in Figure 2.2a. Together, Figure 2.2a and 2.2b show that as modern optical systems move to shorter wavelengths to increase I_0, aero-optical aberrations cause a much more serious degradation of the Strehl ratio, illustrating why aero-optical considerations are critical in the development of any airborne optical system.

Figure 2.3 shows the $\mathrm{OPD_{RMS}}$ necessary to achieve various Strehl ratios over a range of wavelengths. As the wavelength of light decreases the required $\mathrm{OPD_{RMS}}$ decreases linearly for a fixed Strehl ratio.

2.1.1 Typical Optical Wavefront Measurement System

2.1.2 A Brief History of Aero-Optics

The field of aero-optics began with an investigation by Liepmann [21] into the limits of sensitivity of schlieren systems when used in high-speed flow analysis. Liepmann used geometric optics to analyze a small-diameter beam and derive its mean-squared fluctuating deflection angle, $\langle \theta^2 \rangle$. Liepmann propagated the beam in the y direction and assumed the index of refraction changes in

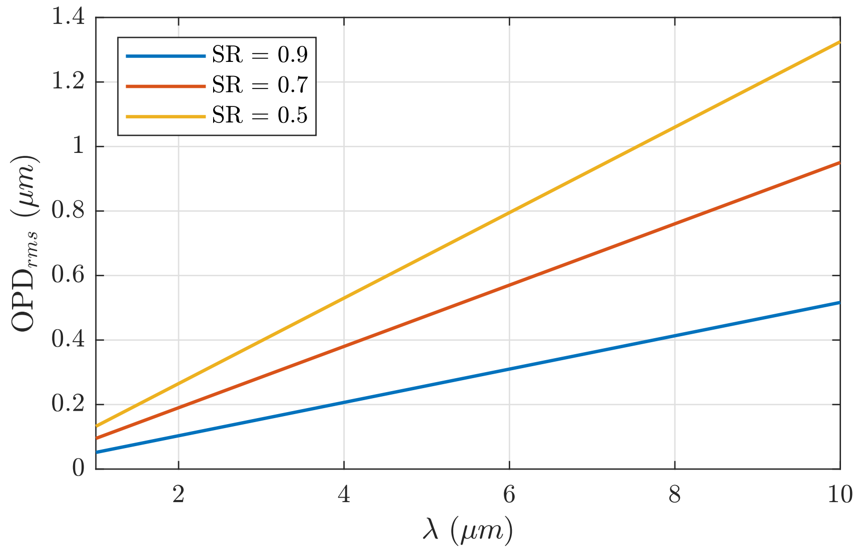

Figure 2.3. OPD$_{\mathrm{RMS}}$ values necessary to obtain Strehl ratios of 0.9, 0.7, and 0.5 over a range of wavelengths.

the $x - z$ plane were statistically similar. Liepmann's analysis for a boundary layer of thickness δ resulted in

$$\langle \theta^2 \rangle = \frac{1}{[n_0(\delta)]^2} \int_0^\delta \int_0^\delta n_0(y) n_0(\zeta) \left\langle \left(\frac{\partial \nu}{\partial y} \right)^2 \right\rangle R_v(|y-\zeta|) dy d\zeta \tag{2.13}$$

where the index of refraction is determined from $n = n_0(y)(1+\nu)$ and $R_v(|y-\zeta|)$ is the correlation function for the index variation. This analysis introduced the concept of a linking equation that allows one to predict time-averaged optical degradation to turbulent flow statistical measurements.

2.2 Acoustics

2.2.1 Basic Acoustics

Starting with the conservation of mass,

$$\frac{\partial \rho}{\partial t} + \nabla \cdot (\rho \mathbf{u}) = 0, \tag{2.14}$$

and separating the density into a time-averaged (ρ_0) and fluctuating portion (ρ'), $\rho = \rho_0 + \rho'$. The fluctuating conservation of mass equation is obtained by separating the density ($\rho = \rho_0 + \rho'$) into a

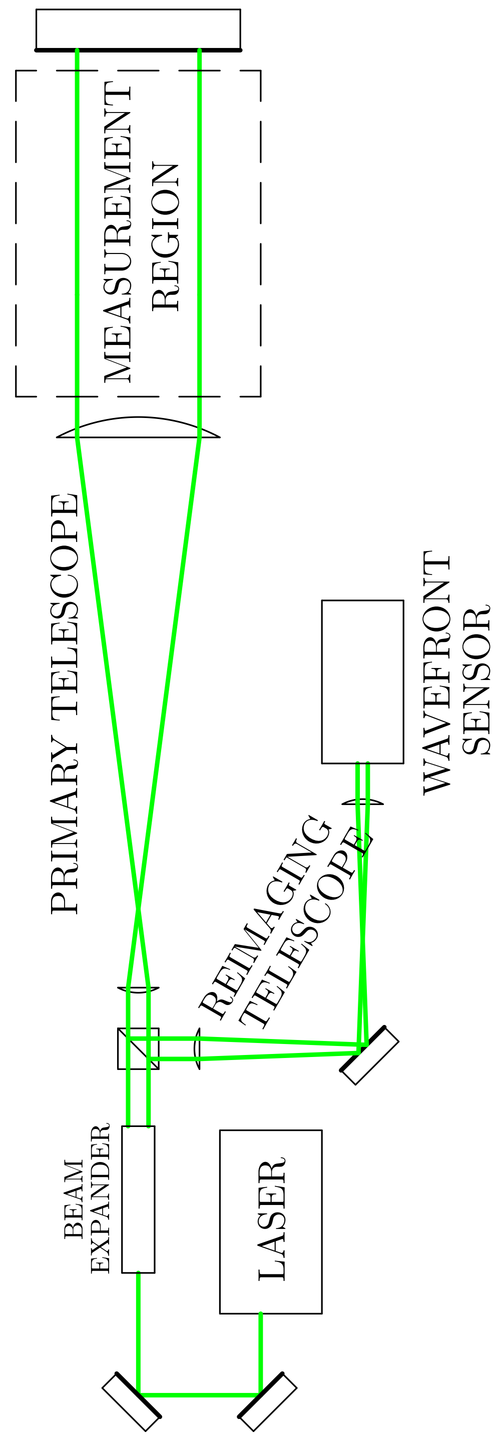

Figure 2.4. Typical double-pass optical wavefront measurement setup.

temporally averaged density, ρ_0, and a

$$\frac{\mathbf{D}\rho'}{\mathbf{Dt}} + \nabla \cdot (\rho_0 \mathbf{u}) = 0 \tag{2.15}$$

For acoustics waves of frequency less than 10^9 Hz the compression of the fluid can be assumed to be adiabatic [25].

$$\left.\frac{\partial p}{\partial \rho}\right|_s = c_0^2 \tag{2.16}$$

2.2.2 Duct Acoustics

Acoustic waves are often enclosed inside of somesort of structure. This section will look at acoustics when confined to a duct in which the acoustic waves primarily travel along one-axis and have walls confining the acoustics along the other two axes as is the case inside of a wind tunnel. Figure 2.5 shows the diagram used for deriving the acoustic properties inside of a constant area duct.

This derivation is primarily influenced from Munjal [26] along with Jacobsen and Juhl [15]. The primary assumption used in this derivation is that the duct is of constant cross-section. This means that all mean quantities (ρ_0, $\mathbf{u_0}$, ...) a constant throughout space and time. Starting with the linearized inviscid forms of the conservation of mass,

$$\frac{\mathbf{D}\rho}{\mathbf{Dt}} + \rho_0 \nabla \cdot \mathbf{u} = 0, \tag{2.17}$$

and conservation of momentum,

$$\rho_0 \frac{\mathbf{Du}}{\mathbf{Dt}} + \nabla p = 0. \tag{2.18}$$

The definition of the speed of sound (Equation 2.16) is then substituted into Equation 2.17,

$$\frac{1}{c_0^2} \frac{\mathbf{D}p}{\mathbf{Dt}} + \rho_0 \nabla \cdot \mathbf{u} = 0, \tag{2.19}$$

where c_0 is the speed of sound at average fluid properties (ρ_0, p_0, T_0, ...). Next the difference between the material derivative ($\mathbf{D}/\mathbf{Dt}$) of Equation 2.19 and the partial derivative ($\partial/\partial \mathbf{x}$) of Equation 2.18 with respect to space is taken which results in the convected 3-D wave equation,

$$\left(\frac{\mathbf{D}^2}{\mathbf{Dt}^2} - c_0^2 \nabla^2 \right) p = 0. \tag{2.20}$$

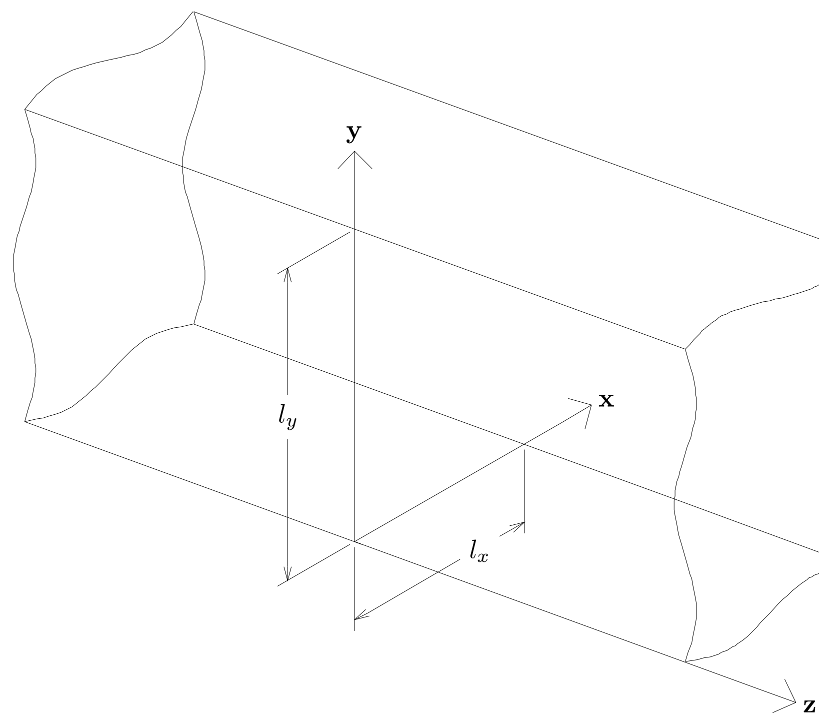

Figure 2.5. Duct with a rectangular cross-section.

Expanding the material derivative and dividing by c_0^2,

$$\left(\frac{1}{c_0^2}\frac{\partial^2}{\partial t^2} + \frac{2\mathbf{M}}{c_0}\frac{\partial^2}{\partial t \partial \mathbf{x}} - (1-\mathbf{M}^2)\nabla^2\right) p = 0, \tag{2.21}$$

where $\mathbf{M} = \mathbf{u_0}/c_0$. By using the fact that $c_0 = \omega/k_0$, Equation 2.20 can be written in a more convent form,

$$\left(\frac{1}{\omega^2}\frac{\partial^2}{\partial t^2} + \frac{2\mathbf{M}}{\omega k_0}\frac{\partial^2}{\partial t \partial \mathbf{x}} - \frac{1-\mathbf{M}^2}{k_0^2}\nabla^2\right) p = 0, \tag{2.22}$$

where ω is the angular frequency and k_0 is the total wavenumber.

At this point the pressure field is going to written in a complex form and assumed to be separable in both time and space such that $\hat{p}(\mathbf{x}, t) = \hat{p}(x, y)\hat{p}(z)\hat{p}(t)$. The temporal solution is assumed to take the form

$$\hat{p}(t) = \exp\{j\omega t\}. \tag{2.23}$$

This results in the spatial component of the convecting wave equation

$$\left((1-\mathbf{M}^2)\nabla^2 - 2jk_0\mathbf{M}\nabla + k_0^2\right)\hat{p}(x, y)\hat{p}(z) = 0. \tag{2.24}$$

This can be further split into axial and cross-sectional components by splitting k_0 into components,

$$k_0 = \sqrt{k_{xy}^2 + k_z^2}, \tag{2.25}$$

and because the mean flow is only in the axial direction ($\mathbf{M} = M\hat{\mathbf{k}}$). The cross-sectional component is a typical Helmholtz equation

$$\left(\frac{\partial^2}{\partial x^2} + \frac{\partial^2}{\partial y^2}\right)\hat{p}_{xy}(x,y) + k_{xy}^2\hat{p}(x,y) = 0, \tag{2.26}$$

whos solution,

$$\hat{p}(x,y) = \Psi_m(x,y), \tag{2.27}$$

is one of infinity many eigen-function solutions with discrete wavenumbers, k_m. The axial component of the convecting wave equation,

$$(1-M^2)\frac{\partial^2\hat{p}(z)}{\partial z^2} - 2jk_0M\frac{\partial\hat{p}(z)}{\partial z} + k_z^2\hat{p}(z) = 0, \tag{2.28}$$

retains the total wavenumber in second term which means its solution will depend on the cross-sectional wavenumber value at cross-sectional mode. The solution to the axial convecting wave equation,

$$\hat{p}(z) = p_m^+ \exp\left\{-jk_{zm}^+ z\right\} + p_m^- \exp\left\{+jk_{zm}^- z\right\}, \tag{2.29}$$

has waves traveling in both directions with the axial wavenumber in each direction for a given mode

$$k_{zm}^{\pm} = \frac{\mp Mk_0 + \sqrt{k_0^2 - (1-M^2)k_m^2}}{1-M^2}. \tag{2.30}$$

The solution for a three-dimensional acoustic wave in a duct with a constant but arbitrary cross-section in complex pressure is the combination of the component solutions presented in Equations 2.23, 2.27, and 2.29,

$$\hat{p}(x,y,z,t) = \Psi_m(x,y)\left(p_m^+ \exp\left\{-jk_{zm}^+ z\right\} + p_m^- \exp\left\{+jk_{zm}^- z\right\}\right)\exp\left\{j\omega t\right\}. \tag{2.31}$$

The two solutions for a plane wave ($\Psi_m = 1$, $k_m = 0$) traveling in a duct have a characteristic speed of $u \pm c_0$. Acoustic modes will travel indefinitly if $k_0^2 - (1-M^2)k_m^2 > 0$ (the quantity inside of the square-root of Equation 2.30). This presents a frequency at which a given mode will cut-on,

$$f_{cuton} = \frac{c_0}{2\pi}\sqrt{(1-M^2)k_m^2}. \tag{2.32}$$

Below this frequency, an acoustic mode will be exponentially attenuated as it travels throught the duct.

2.2.2.1 Characteristic Equations of Cross-Sections

In order to determine the characteristic equations of an acoustic field within a cross-section the solution to Equation 2.26 needs to be determined. A typical boundary condition that is used in the solution of this 2-D Helmholtz equation is using the assumption that the walls are rigid.

$$\nabla p_{x,y}(x,y) \cdot \mathbf{n}_{wall} = 0 \tag{2.33}$$

This boundary condition results in the acoustic waves being perfectly reflected off of the duct walls. There are several known empirical solution sets of the characteristic equations for specific geometry with the rigid wall assumption.

The first of these solutions is for a rectangular cross-section,

$$\Psi_{m,n}(x,y) = \cos(k_x x)\cos(k_y y), \tag{2.34}$$

where the wave numbers along each axis are $k_x = m\pi/l_x$ and $k_y = n\pi/l_y$. The duct has a width of l_x and a height of l_y. The total cross-sectional wave number for use in determining the axial wave numbers is

$$k_m^2 = k_x^2 + k_y^2. \tag{2.35}$$

Figure 2.6 shows the characteristic functions when m=0:2 and n=0:3 for a rectangular cross-section of width of l_x and height of l_y. The lines depicted in the figure are nodal lines and represent locations where there is zero pressure fluctuations for that acoustic mode.

The second set of known empirical solutions is for a circular cross-section with radius R,

$$\Psi_{m,n}(r,\theta) = J_m(k_{mn}r)\exp\{\pm jm\theta\}, \tag{2.36}$$

where J_m is the m^{th} Bessel function of the first kind and the $\pm$ indicates the direction of spin. If

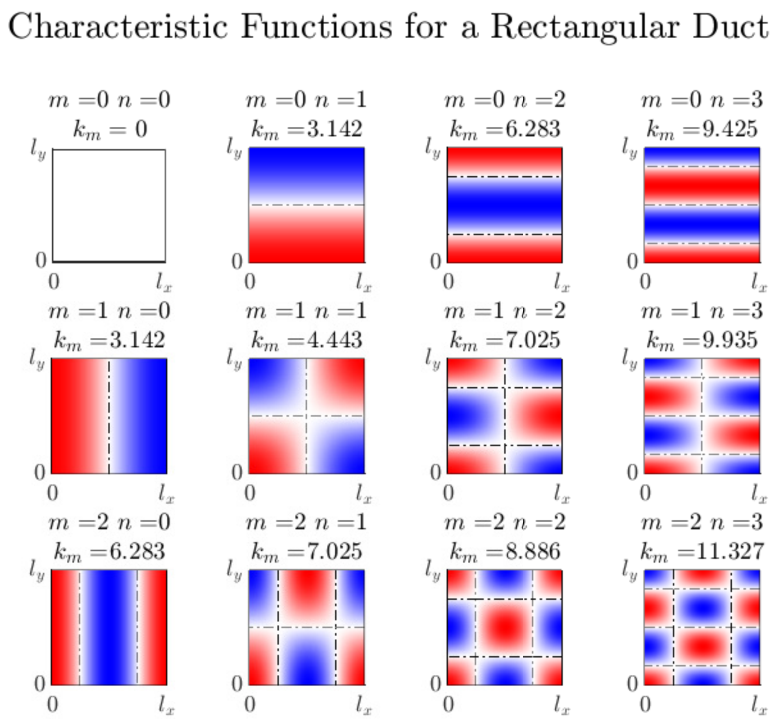

Figure 2.6. Characteristic solutions to Equation 2.26 with rigid wall in a rectangular cross-section where m=0:2 and n=0:3. Nodal lines are depicted by the dot-dash lines. The cross-sectional wave numbers, k_m, listed are for a duct of unit length and height.

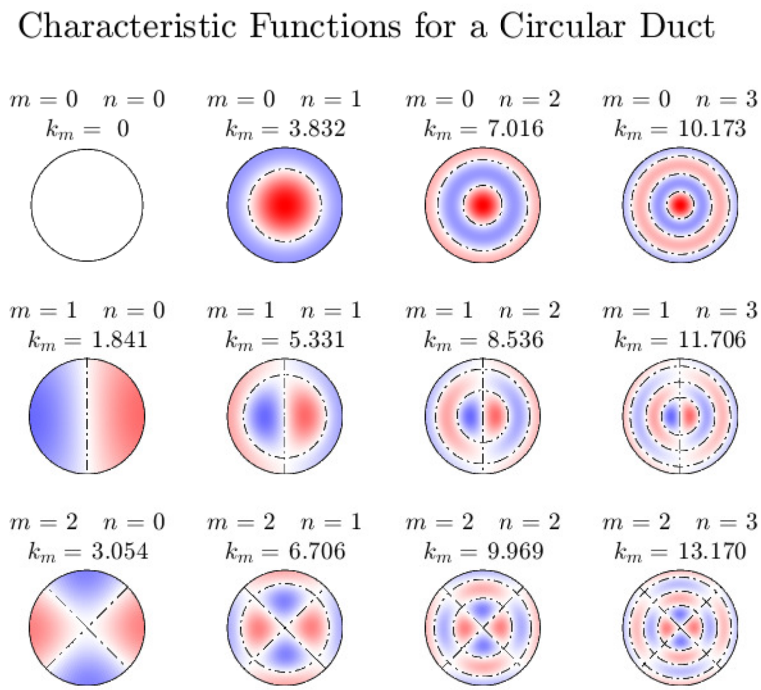

Figure 2.7. Characteristic solutions to Equation 2.26 with rigid wall in a circular cross-section where m=0:2 and n=0:3. Nodal lines are depicted by the dot-dash lines. The cross-sectional wave numbers, k_m, listed are for a duct of unit radius.

the left and right spin coefficients are equal in magnitude then a non-spinning mode is created. In order to satisfy the solid wall boundary condition $J'_m(k_{mn}R) = 0$ which determines a set of discrete values for the cross-sectional wave number at the n^{th} zero for the m^{th} Bessel function. Figure 2.7 shows the characteristic functions for a circular duct.

CHAPTER 3

AERO-OPTICAL AND ACOUSTICAL COUPLING

- Spherical solutions and measurements
- Double check microphone and preamp models and settings
- Mode marching method

Acoustic waves are isentropic compression waves with the fluctuating pressure, p', determining the strength of the wave. This fluctuating pressure is related to the sound pressure level, SPL by

$$\mathrm{SPL} = 20 \log_{10}\left(\frac{p_{rms}}{p_0}\right) \tag{3.1}$$

where p_{rms} is the root mean square of the pressure fluctuation, and p_0 is the reference pressure (20 μPa for air). The pressure fluctuations can be converted to the density fluctuations via the definition of the speed of sound:

$$c_0^2 = \left(\frac{\partial p}{\partial \rho}\right)_s = \frac{p'}{\rho'} \tag{3.2}$$

where c_0 is the speed of sound at mean fluid properties and the subscript s denotes constant entropy. It can be shown by combining Equations 2.5 and 2.7 that the fluctuating density can be related to the OPD,

$$\mathrm{OPD} = K_{GD} \int_{s_1}^{s_2} \rho' ds. \tag{3.3}$$

This can be combined with Equation 3.2,

$$\mathrm{OPD} = \frac{K_{GD}}{c_0^2} \int_{s_1}^{s_2} p' ds, \tag{3.4}$$

to provide a way of computing the optical path difference of a pressure field.

3.1 Simulating an Optical Wavefront Measurement from an Acoustic Field Function

An optical wavefront can be simulated from a complex pressure field by applying Equation 3.4. To accomplish this, two separate coordinate systems will need to be defined. The first is the beam coordinate system, $\mathbf{x}_B$, that will have a measurement aperture, which is typically circular, defined in the xy-plane and propagates in the z-direction. The second is the acoustic coordinate system, $\mathbf{x}_A$, that will be defined based on the source location or the geometry that the acoustic waves are propagating through. These to coordinate systems will have a function representing a transform from one to the other

$$\mathbf{x}_A = R\mathbf{x}_B + T, \tag{3.5}$$

where R is a matrix which represents the rotation and T is a vector that represents the translation.

The important parameters for defining the aperture which the beam coordinate system is based are the aperture size, Ap, and the number of lenslets or sub-apertures, $N_{lenslets}$. Assuming that the aperture is either circular or square and the lenslet size and sub-aperture size is approximately $Ap/N_{lenslets}$, the x locations of the center of the sub-apertures go from $-Ap/2(1 - 1/N_{lenslets})$ to $Ap/2(1 - 1/N_{lenslets})$ by steps of $Ap/N_{lenslets}$ with the y locations having the same values. This gives a matrix representing both x_{Ap} and y_{Ap} that is $N_{lenslets}$ by $N_{lenslets}$. For the purpose of removing piston, tip, and tilt and creating a mask that represents the beam aperture, the radial coordinates, ρ_{Ap} and θ_{Ap}, of the aperture should also be calculated. A circular beam will have a mask defined by,

$$Mask_{Ap} = \begin{cases} 1, & \text{if } \rho_{Ap} \leq Ap/2 \\ 0, & \text{otherwise.} \end{cases} \tag{3.6}$$

The beam coordinate frame is the aperture coordinates extruded in the z-direction over the range of desired z-values.

After the beam coordinates are transformed into the acoustic coordinates using Equation 3.5, the complex pressure field, $\hat{p}(x, y, z, t)$ can be calculated at the points that are within the optical beam. If the pressure field is separable into spatial and temporal components, than the integration along the beam length only needs to be done once for each temporal frequency,

$$\widehat{\mathrm{OPD}}(x, y) = \frac{K_{GD}}{c_0^2} \int_{z_1}^{z_2} \hat{p}(x, y, z)_{Ap} dz, \tag{3.7}$$

where $\widehat{\mathrm{OPD}}(x, y)$ is the complex optical path difference as measured in the aperture plane. If a complex density field is known instead, than Equation 3.7 becomes

$$\widehat{\mathrm{OPD}}(x, y) = K_{GD} \int_{z_1}^{z_2} \hat{\rho}(x, y, z)_{Ap} dz. \tag{3.8}$$

For the purposes of calculating temporally mean optical properties of simulated beam passing through a known complex pressure or density field a phase vector was defined, $\phi = [0, 2\pi)$. The measurable component as a function of phase is

$$\text{OPD}(x, y, \phi) = \text{REAL}\left[\widehat{\text{OPD}}(x, y)\exp\{-j\phi\}\right], \tag{3.9}$$

or as a function of time for all temporal frequencies,

$$\text{OPD}(x, y, t) = \text{REAL}\left[\sum \widehat{\text{OPD}}(x, y)\exp\{-j\omega t\}\right], \tag{3.10}$$

where there is a separate $\widehat{\text{OPD}}(x, y)$ computed for each temporal frequency. One of the more important measurements that can be calculated from OPD is the spatial RMS, OPD_{RMS}, which is calculated at each time or phase step at the points where the aperture mask equals one.

3.2 Simple Examples of Acoustic-Optical Coupling

Two basic acoustic pressure fields will be numerically examined for their optical properties. The first will be a planar acoustic wave that will be numerically simulated over a variety of conditions. The second will be a spherical acoustic wave that will be both numerically simulated and validated experimentally.

3.2.1 Planar Acoustic Waves

A planar wave is the simplest solution to the wave equation and varies only in time and the direction of travel. A planar wave can be calculated from the set of solutions for duct acoustics, Equation 2.31, given that $\Psi_m(x, y) = 1$,

$$\hat{p}(z, t) = p_m \exp\left\{j(\omega t \mp k_{zm}^{\pm} z)\right\}. \tag{3.11}$$

This section will show several plots to show the effect that acoustic waves have on the optical wavefront of a planar wave with the general geometry shown in Figure 3.1. For the following example, l_n is the width of the acoustic disturbance (for example, the width of the wind tunnel), θ is the angle between the planar acoustic wave and the beam direction, A_p is the aperture diameter of the beam, and Λ is the wavelength of the acoustic wave.

Figure 3.2 shows the time averaged OPD_{RMS} per meter of beam propagation when the beam

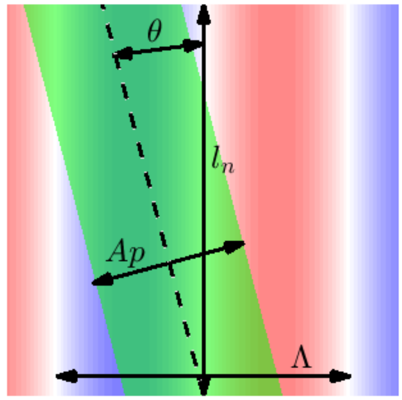

Figure 3.1. General geometry for various sample calculations for showing the acoustic-optical coupling effect.

path is parallel ($\theta = 0$) to the peaks and troughs of the planar acoustic wave as SPL is varied. As the sound pressure level increases the time averaged $\mathrm{OPD}_{\mathrm{RMS}}$ also increases and can easily reach the point of being a significant factor in the measured optical disturbance. There is little difference between 0.1 and 1 Λ/Ap, but as the wavelength gets much larger compared to the beam diameter, then the optical effect of the noise is greatly reduced, this effect is known as aperture filtering [37].

Aperture filtering is more clearly shown in Figure 3.3. As the Λ/Ap ratio increases from 0.1, time-averaged $\mathrm{OPD}_{\mathrm{RMS}}$ remains fairly constant until it starts to drop around Λ/Ap of 0.7 and starts to asymptotically approach zero which it basically reaches by Λ/Ap of 10. Figure 3.3 also shows the effect of changing the beam angle, θ, through the acoustic field. For nonzero θ, the beam encounters alternating high and low index of refraction as it passes through the test region, so that the time-averaged $\mathrm{OPD}_{\mathrm{RMS}}$ begins to decrease compared to the $\theta = 0°$ case below $\Lambda/Ap = 1$. There are also points of zero optical disturbance that occur at $\theta_{zero} = \tan^{-1}(n\Lambda/l_n)$ for $n \neq 0$; these points occur because the peaks and valleys of the optical disturbance caused by the sound wave effectively cancel out over the length of the integration path, $l_n/\cos\theta$.

Figures 3.2 and 3.3 show the optical effect of plane acoustic waves in a no-flow environment. The effect of wind-tunnel flow is to stretch (downstream-traveling waves) or compress (upstream-traveling waves) the wavelength of the acoustic noise thereby altering the filtering effect of the beam aperture. Figure 3.4 shows a typical optical disturbance from the two transverse acoustic waves (u+c and u-c) present in a wind tunnel at Mach 0.6. Both waves have a RMS sound

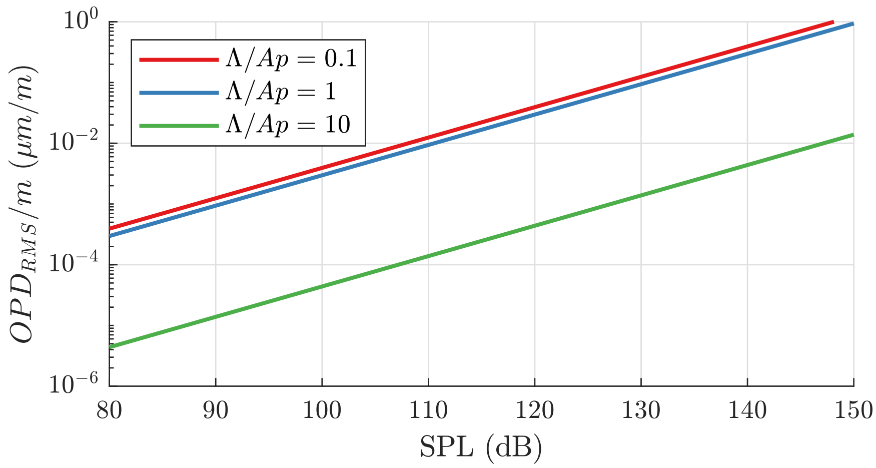

Figure 3.2. Theoretical time-averaged OPD_{RMS} per meter of beam propagation as a function of sound pressure level, SPL, for several Λ/Ap ratios and $\theta = 0$.

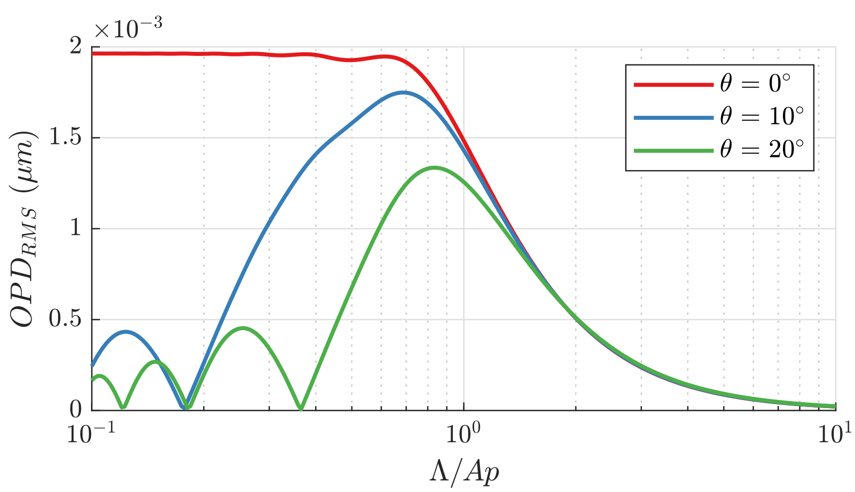

Figure 3.3. Theoretical time-averaged OPD_{RMS} for a rms sound pressure of 1 Pa (SPL of 94 dB), l_n of 1 m, and various angles and Λ/Ap ratios.

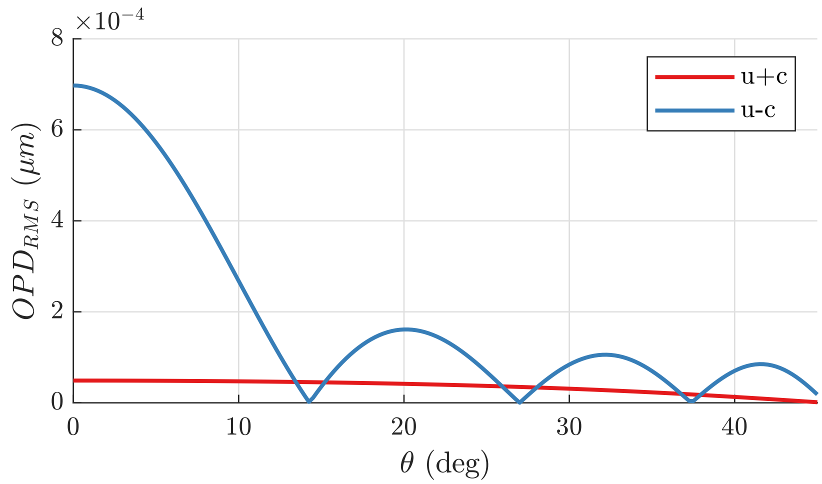

Figure 3.4. Theoretical time-averaged OPD_{RMS} for the two acoustic waves (u+c and u-c) for the blade pass frequency (534 Hz) at Mach 0.6 with a RMS sound pressure of 1 Pa (SPL of 94 dB), l_n of 1 m, and Ap of 15 cm.

pressure of 1 Pa and the beam has an aperture of 15 cm and propagates through a 1 m acoustic field inside the tunnel. Over a vast majority of the look back angles the upstream-traveling acoustic wave has a much greater effect on the optical disturbance compared to the downstream-traveling acoustic wave, due to the much shorter wavelength of the upstream-traveling waves which is less affected by aperture filtering. However, the upstream-traveling wave goes through several zero points so the downstream-traveling wave dominates at some look back angles.

3.2.2 Spherical Acoustic Waves

The acoustic field from an speaker maybe assumed to be a spherical wave from a pulsating point if the frequency is sufficiently low and measurement region is far enough away from the source [30]. This pressure field when converted to complex pressure is represented by

$$\hat{p}(r,t) = \frac{A_0}{r} \exp\left\{-j(kr - \omega t)\right\}, \tag{3.12}$$

where A_0 is the fluctuating pressure strength and r is the distance from the source to the measurement point. The RMS pressure of this field can be represented by

$$p_{rms} = \frac{|A_0|}{r\sqrt{2}}. \tag{3.13}$$

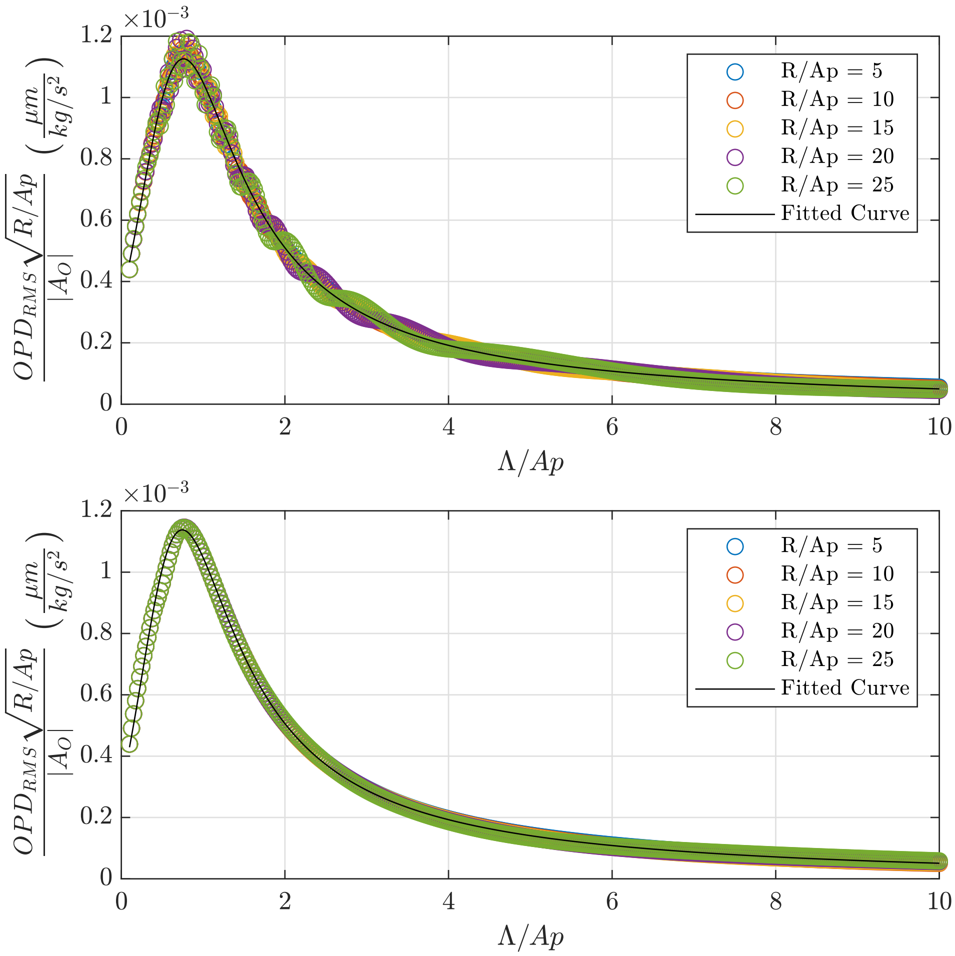

Figure 3.5. Theoretical time-averaged $\mathrm{OPD}_{\mathrm{RMS}}$ for a spherical acoustic wave. The top plot shows a perfect spherical acoustic signal integrated over ±5-m. The bottom plot shows has a Tukey window applied along the beam length to partially emulate source directivity which significantly reduces the measured oscillations.

3.2.2.1 Theoretical OPD Measurements

A set of optical properties where calculated for a beam passing through a spherical acoustic field as defined by a point source using the process described previously in Chapter 3.1. These calculations used an circular aperture size of 0.25-m in diameter consisting of 32x32 sub-apertures, an acoustic wavelength, Λ, of $Ap/4$ to $10Ap$, and a distance from the point source to the center of the aperture, R, of $5Ap$ to $25Ap$. The beam was integrated over ±5-m from the plane of the point source with 25 phase step used to calculate mean values.

The result of these simulated acoustic fields is shown in Figure 3.5. The top plots shows the expected optical disturbance ratio, $\mathrm{OPD}_{\mathrm{RMS}}/|A_0|$, for a perfectly spherical acoustic field measured

TABLE 3.1

CURVE FIT VALUES FOR FIGURE 3.5 AND EQUATION 3.14

Coefficent	Value
p_1	-1.845e-05
p_2	4.769e-04
p_3	4.520e-03
p_4	1.435e-03
q_1	5.399e+00
q_2	-5.145e+00
q_3	4.869e+00

over the beam length. With the exception of some oscillations that are caused by end effects in the integration. The oscillations can be greatly reduced by using a windowing function in the z-direction such as a Hanning or Tukey window which also can be used to roughly model directivity of the speaker's acoustic emission as shown in the bottom plot. While this plot was calculated with a single aperture diameter, the general trend holds for all other aperture diameters that were tested, the only effect was the size and width of the oscillations.

The peak of the optical disturbance ratio, $\mathrm{OPD}_{\mathrm{RMS}}/|A_0|$, is located at $\Lambda/Ap \approx 0.75$ for a circular aperture. The signal is reduced above this value due to aperture filtering and below this value because the shorter wavelength have a reduced distance before alternating high and low index-of-refraction regions reduce the optical path difference. When the acoustic source point is sufficiently far enough away from the measurement beam, $R/Ap \geq 2$, the optical disturbance ratio, $\mathrm{OPD}_{\mathrm{RMS}}/|A_0|$ when multiplied by $\sqrt{R/Ap}$, can be collapsed onto a single curve for a range of Λ/Ap of 0.1 to 10. Above $\Lambda/Ap = 10$ the curves start to diverge away from one another. An approximate function fit to this data is

$$\frac{\mathrm{OPD}_{\mathrm{RMS}}\sqrt{R/Ap}}{|A_0|} \approx \frac{p_1(\Lambda/Ap)^3 + p_2(\Lambda/Ap)^2 + p_3(\Lambda/Ap) + p_4}{(\Lambda/Ap)^3 + q_1(\Lambda/Ap)^2 + q_2(\Lambda/Ap) + q_3} \tag{3.14}$$

with coefficient values shown Table 3.1. This functional fit has a R^2 value of 0.9991.

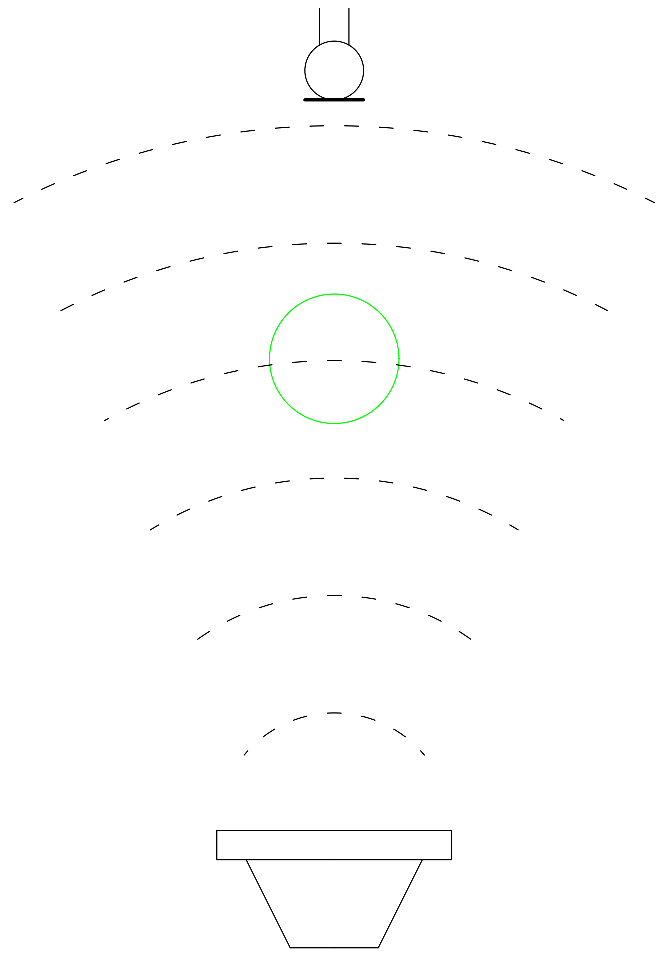

Figure 3.6. Spherical acoustic wave measurement test.

3.2.2.2 Measurement of a Spherical Acoustic Wave with an Optical Beam

A small bench top experiment was used to compare the simultaneous optical and microphone measurements of an acoustic field from a speaker as shown in the measurement plane in Figure 3.6. The distance from center of the beam to the speaker was 102-mm with a beam diameter of 28-mm. An ACO model 7016B microphone [8] was placed directly over the speaker at a distance of 158-mm and was used with a Brüel & Kjær model 2670 preamplifier [4]. The speaker in use was Peerless model XT25SC90-04 [28] which has a fairly flat on-axis response from 1-kHz to 40kHz.

The wavefront measurements system utilized in these measurements is similar to that shown in Figure 2.4 except there was no primary telescope. The speaker was located in the center of the measurement region which was about 2-feet in length and the re-imaging telescope reduced

TABLE 3.2

COMPARISON OF MICROPHONE AND WAVEFRONT COMPUTATION OF $|A_0|$

$f_{speaker}$ (Hz)	$V_{speaker}$ (mV)	p_{rms} (Pa)	OPD$_{RMS}$ (μm)	$\|A_0\|_{mic}$ (kg/s^2)	$\|A_0\|_{wf}$ (kg/s^2)	Diff (%)
9000	100	5.65	6.545e-04	1.26	1.55	20.38
9000	250	12.23	1.421e-03	2.73	3.36	20.56
9000	500	19.52	2.386e-03	4.36	5.64	25.62
14000	1250	5.20	6.831e-04	1.16	1.18	1.24
14000	250	9.33	1.230e-03	2.09	2.12	1.50
14000	375	9.68	1.272e-03	2.16	2.19	1.16
18000	125	3.73	4.987e-04	0.83	0.84	1.10

the beam diameter by a factor of two and re-imaged the return mirror. Optical wavefronts and microphone measurements were taken at 49-kHz. The speaker was sinusoidally excited at three different frequencies (9, 14, and 18-kHz) at a variety of voltages.

The absolute value of the fluctuating pressure strength, $|A_0|$, was calculated two different ways. The power spectra of the microphone data was used to calculate the average p_{rms} at the excitation frequency and the fluctuating pressure strength using Equation 3.13. The optical wavefront was band-pass filtered at the excitation frequency using a process that will be discussed in Chapter **??**. The time averaged OPD$_{\mathrm{RMS}}$ was used to calculate the fluctuating pressure strength using Equation 3.14.

The results of these measurements of the fluctuating pressure strength is shown in Table 3.2. The differences between the two techniques for measuring the fluctuating pressure strength fell into two groups. For the 9-kHz cases, the differences ranged from 20-26% while the higher frequency cases the differences were between 1.1-1.5% and in all cases the wavefront measurement reported a higher fluctuating pressure strength. With the exception of the highest excitation case at 9-kHz, the differences between the to techniques was fairly constant for each frequency group. Some of these differences maybe attributable to the frequency response of the microphone.

Measured and simulated wavefronts for the highest excitation cases at each frequency are shown in Figure 3.7. The 9-kHz case shows some anomalies on the measured wavefront on the right

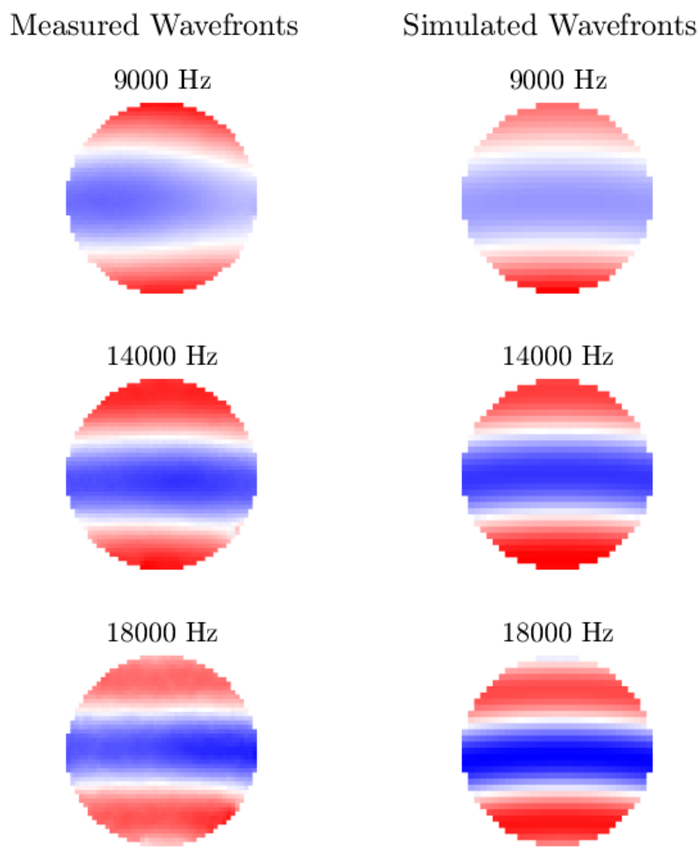

Figure 3.7. Comparison of some of the measured wavefronts and simulated ones.

side, deviating from spherical wave significantly likely contributing the significantly higher estimated pulsating field strength value when compared to the microphone estimate. The 14 and 18-kHz cases show some remarkable agreement between the measured and simulated images. Optical wavefront measurements can be utilized for making non-intrusive acoustic field measurements espically when the acoustic field is simple.

3.3 Estimating the Acoustic Field Inside the Test-Section

3.3.1 Mode Marching Process

1. Start with a known or assumed source acoustic field, $p^n(x, y)$
2. Calculate the transmitted pressure ratio
   - Traveling with subsonic flow
   $$\frac{p^t}{p^i} = \left(\frac{1 + M_n}{1 + M_{n+1}}\right)\left(\frac{2M_{n+1}}{M_n + M_{n+1}}\right)\left(\frac{X_{n,n}}{X_{n,n+1}}\right)\left(\frac{X_{n,n}}{X_{n+1,n+1}}\right)^{1/(\gamma-1)} \tag{3.15}$$
   - Traveling against subsonic flow
   $$\frac{p^t}{p^i} = \left(\frac{1 - M_n}{1 - M_{n+1}}\right)\left(\frac{2M_{n+1}}{M_n + M_{n+1}}\right)\left(\frac{X_{n,n}}{X_{n,n+1}}\right)\left(\frac{X_{n,n}}{X_{n+1,n+1}}\right)^{1/(\gamma-1)} \tag{3.16}$$
   - Where
   $$X_{a,b} = 1 + \frac{\gamma - 1}{2} M_a M_b \tag{3.17}$$
3. March acoustic field to next axial step,
$$p^{n+1}(x, y) = p^n(x, y)\frac{p^t}{p^i}\exp\{j(\omega t \mp k^{\pm}_{zm} z)\} \tag{3.18}$$
4. Best-fit set of local duct modes coefficients, C_m, to acoustic field $p^{n+1}(x, y)$
5. Calculate new acoustic field from duct mode and repeat from step 2
$$p^n(x, y) = \sum_{m=0}^{M} C_m \cdot p_m(x, y) \tag{3.19}$$
6. When the end point is reached, step inlet acoustic field (rotate fan) and repeat

CHAPTER 4

DISPERSION ANALYSIS

I think an analytical solution maybe needed for the n-dimensional case. Either a n-dimensional tophat function or dirac delta function. I also plan on adding a little analysis on viewing angle in the test-section.

Dispersion analysis is an expansion of power spectra analysis from one-dimension to n-dimensions. The technique allows a signal that is measured in both time and space to be separated into not only temporal-frequency components but also spacial-frequency components. This allows not only the direction of travel that a particular wave to be determined but also the velocity of which that the wave travels. The benefits of using a dispersion analysis are shown in Figure 4.1. The single row of sub-apertures from a wavefront measurement conducted with a 5-inch diameter beam propagating normally through two boundary layers with a free-stream Mach number of 0.5. This measurement was preformed in the University of Notre Dame Whitefield Wind Tunnel in a test section that contained a model representing the fuselage of the AAOL aircraft [18] with window that was flat and flush to the outer mold line of the fuselage. The top plot shows a traditional power spectra representation averaged over the row of data. Both the blade-passing frequency (517-Hz) and its sub-harmonic had similar power levels with an additional five harmonics showing significant spikes above the local baseline measurement. There are three additional strong peaks at approximately 3100, 4850, and 5850 Hz that do not have an easily identifiable source or explanation.

Both the middle and bottom plots show a dispersion plot or two-dimensional power spectra measurement. The colorbars were intentionally not shown in order to allow for all three plots to be aligned in the temporal frequency axis and the color space is representative of the power spectra in log-space. The middle plot shows horizontally moving waves with the y-axis representing the spatial frequency, ξ_x, with units of inverse meters. Waves with positive spatial frequencies are moving in the direction of flow. All of the temporal frequency below 2000-Hz, where there is an obvious separation between the upstream and downstream traveling optical disturbances, are significantly more on the upstream traveling side. The blade-passing frequency and its various harmonics show some significant broadband spatial frequency signals. The three signals of unknown origin are

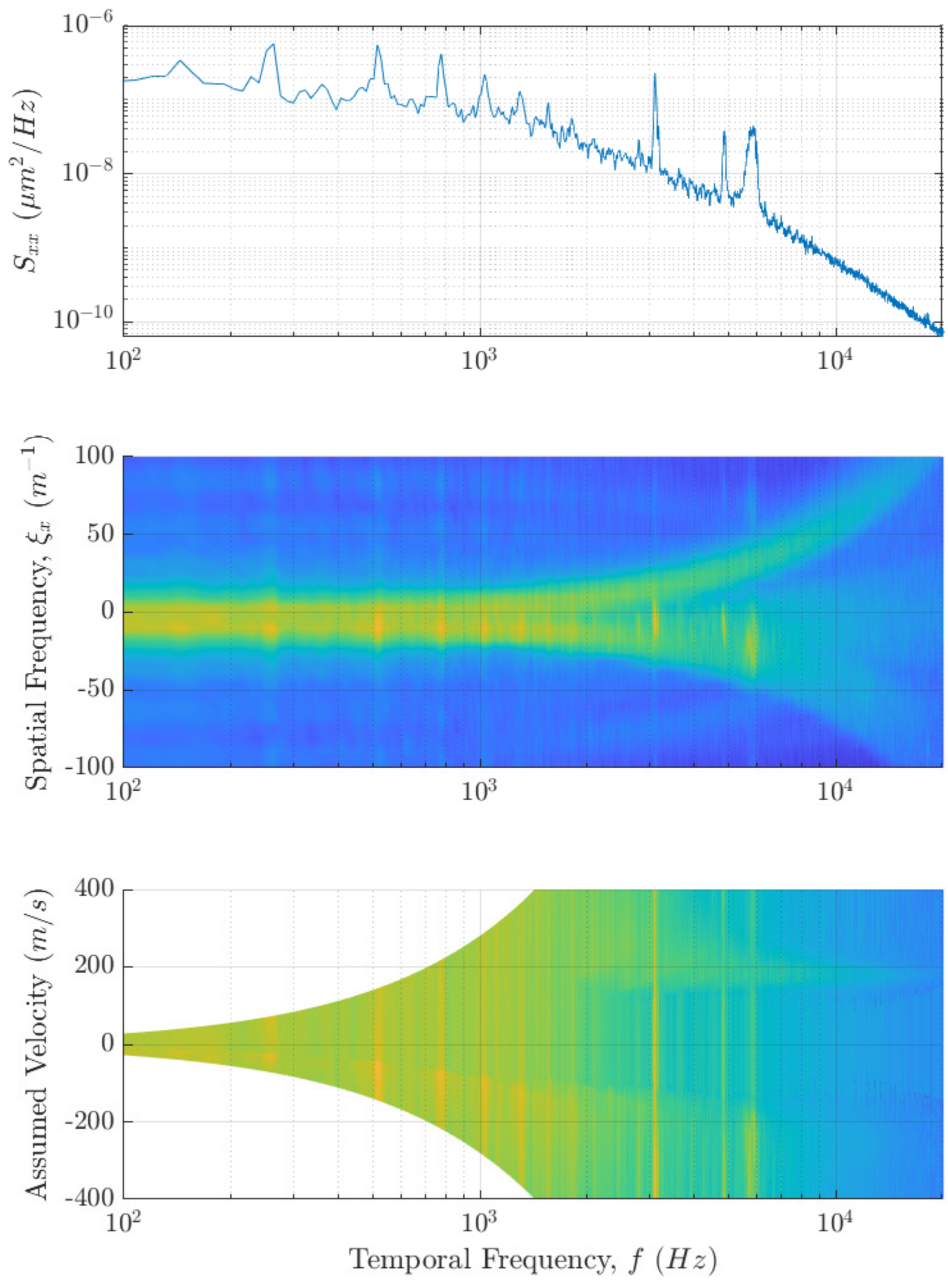

Figure 4.1. Dispersion plot example and comparison to traditional power spectra measurements. A single row of a wavefront measurement was used in this example. The top plot shows the typical power spectra measurement averaged over the entire row of data. Both the middle and bottom plots show the dispersion plot with the y-axis as spacial-frequency in the middle and velocity in the bottom assuming $u = f/\xi_x$.

clearly moving upstream but also show some significant broadband spatial signal that is indicative of a source producing optical disturbances that travel in both directions around the tunnel similar to the blade-passing frequency disturbances coming off of the wind tunnel fan. In addition to optical disturbances branching off in the upstream and downstream moving directions there is a significant disturbances along zero spatial frequency representing a collection of standing waves.

The bottom plot shows the same dispersion plot as the middle one but with the y-axis representing an assumed velocity, $u_{assumed}$, where

$$u_{assumed} = \frac{f}{\xi_x}. \tag{4.1}$$

The actual velocity, u, of a disturbance in the dispersion plot would be

$$u = \frac{\partial f}{\partial \xi_x}. \tag{4.2}$$

The assumed velocity measurement is in effect a average of the actual velocity assuming a zero-zero intercept in frequency space. As there was no discernible separation between disturbance the upstream and downstream moving disturbances in the middle plot below 2000-Hz, there is no discernible velocity below that point. The primary optical disturbance moving in the direction of flow is moving at the free-stream velocity of approximately 175-m/s. The upstream traveling disturbance is traveling at the same speed but due to the signal being broader is more difficult to measure this way. When the middle plot is shown with all linear axis, the slope of any given line through the origin is the inverse of the assumed velocity. This is why the disturbances along the zero-spatial frequency line are a collection of standing waves and not some structure with broadband temporal content as it would be traveling at near infinite speed. More discussion will follow a derivation of the dispersion analysis technique which is the n-dimensional power spectra.

4.1 One-Dimensional Power Spectra Calculation

The typical power spectrum calculation on a set of data that is only in one dimension, typically over the temporal dimension. A typical example would be a single sensor measurement over time but a sensor array used to take data at one moment in time could used to measure the power spectrum in terms of spatial frequencies. For a typical single-point measurement that varies in time, $x(t)$, the power spectra calculation is

$$S_{xx} = \frac{|\,\mathrm{FFT}(x(t))|^2}{N \cdot f_s}, \tag{4.3}$$

where FFT is the Fast Fourier Transform, N is the number of samples, and f_s is the sample rate [2]. For data that has only a real component the Fast Fourier Transform function produces magnitude and phase relations at each frequency step, f_s/N, over the range from zero-frequency up to but not including the Nyquist frequency, f_s/w, with a mirrored set of data that can be represented either below (starting at $-f_s/2$) or above (ending just below f_s) this range. The Nyquist frequency not being included and the mirrored data is due to an assumption that is integral to the Fourier Transform, that being the signal is assumed to be periodic.

The total energy, σ^2, of the signal must be preserved through the transform from physical space-time to frequency space

$$\sigma^2 = \frac{\sum x^2(t)}{N} = \Delta f \sum S_{xx}(f). \tag{4.4}$$

Additionally, because of the periodic nature of the Fourier Transform and a finite sample length of discrete data, spectral leakage can cause the power in one frequency bin to leak into adjacent frequency bins. To minimize this spectral leakage, windowing functions are employed which typically force the end points of the signal to zero. The Hann window,

$$w(t) = 1/2 \left[1 - \cos\left(\frac{2\pi t}{T}\right)\right], \tag{4.5}$$

is one of the more commonly used windowing functions where $w(t)$ is the window function, t is the time at a given sample, and T is the total sample time. Since the windowing of a data set changes the signal energy some correction is needed to be applied. For an arbitrary windowing function the correction factor, c_w, can be obtained by substituting the windowing function in place of $x(t)$ in Equation 4.4,

$$c_w = \frac{1}{\sqrt{\sum w^2(t)/N}}. \tag{4.6}$$

For a Hann window this correction factor approaches $\sqrt{8/3}$ as N goes to infinity. When Equation 4.3 is combined with a windowing function and associated correction the double sided power spectra equation in one dimension becomes

$$S_{xx} = \cdot \frac{|c_w \cdot \mathrm{FFT}\{x(t) \cdot w(t)\}|^2}{N \cdot f_s}. \tag{4.7}$$

A simple MATLAB function for computing the power spectrum of a one-dimensional signal with an arbitrary windowing function is shown in Appendix A.1.

4.2 N-Dimensional Power Spectra Calculation

For measurements with multiple spatial and temporal dimensions the Fast Fourier Transform is applied n-times where n is the total number of dimensions, with each application in a different dimension,

$$\mathrm{FFT_n}(x) = \mathrm{FFT}(\mathrm{FFT}(\cdots \mathrm{FFT}(\mathrm{FFT}(x,1),2)\cdots,n-1),n), \tag{4.8}$$

where $\mathrm{FFT}(x,n)$ is the Fast Fourier Transform of x in the n^{th} dimension. For a n-dimensional array the operation becomes,

$$\mathbf{S_{xx}} = \frac{|c_w \cdot \mathrm{FFT_n}\{f(\mathbf{x}) \cdot w(\mathbf{x})\}|^2}{\prod \overrightarrow{N} \cdot \overrightarrow{f_s}}, \tag{4.9}$$

where $\mathbf{S_{xx}}$ is the n-dimensional power spectra array or dispersion array, $f(\mathbf{x})$ is a n-dimensional set of data, $w(\mathbf{x})$ is a n-dimensional windowing function, $\overrightarrow{N}$ is a vector denoting the number of elements in each dimension, $\overrightarrow{f_s}$ is a vector denoting the sample rate in each dimension, and

$$c_w = \frac{1}{\sqrt{\sum w^2(\mathbf{x}) / \prod \overrightarrow{N}}}. \tag{4.10}$$

The signal energy conservation relationship becomes

$$\sigma^2 = \frac{\sum \mathbf{x}}{\prod \overrightarrow{N}} = \prod \overrightarrow{\Delta f_s} \sum \mathbf{S_{xx}}, \tag{4.11}$$

where $\overrightarrow{\Delta f_s}$ is a vector representing the frequency step sizes in each dimension. A simple MATLAB code for calculating the dispersion of x with an arbitrary windowing function is shown in Appendix A.2.

4.3 Non-Rectangular Spatial Windows

For n-dimensional data sets that fill a rectangular array, a windowing function can easily be created by multiplying together a series of one-dimensional windowing functions created in the direction of each dimension. For non-rectangular data sets, such as is often the case with optical wavefront measurement, windowing functions take some additional steps in there construction. In cases when the spatial measurement locations are constant throughout time, the windowing function can be split into two separate components,

$$w(\mathbf{x}) = w_t(t) \cdot w_s(x,y), \tag{4.12}$$

the temporal windowing function, $w_t(t)$, and the spatial windowing function, $w_s(x, y)$. This dissertation uses a Hann window for the temporal windowing function and a modified Hann window for the spatial windowing function. For the case of a circular aperture, the Hann window can be reformulated to be based normalized radius, ρ_N, of the aperture,

$$w_s(\rho_N) = \begin{cases} \frac{1+\cos(\pi \cdot \rho_N)}{2} & \text{if } \rho_N < 1 \\ 0 & \text{otherwise.} \end{cases} \tag{4.13}$$

This modified Hann window is two-dimensional with a value of one at the center of the aperture and decreases to zero at the edge of the aperture in the same manor as a Hann windows decreases from the center to either end.

Because the wavefronts measurements often had a clipped edge or some other obscuration, a different method was employed. For an arbitrary shaped aperture, the minimum distance from any given measurement location to the edge of the aperture was used to create the spatial windows. The minimum distance can be computed given the a set of points (x and y) that spans the measurement range and the set of points outside of the aperture (x_O and y_O),

$$d_{min}(x, y) = \min\left\{\sqrt{(x - x_O)^2 + (y - y_O)^2}\right\}. \tag{4.14}$$

This distance is then normalized by the maximum value and the resulting spatial window given a modified Hann window,

$$w_s(x, y) = \frac{1 + \cos\left\{\pi \cdot (1 - d_{min}^{norm}(x, y))\right\}}{2}. \tag{4.15}$$

This same basic process can be extended to data sets where the locations of measurements in space vary with time.

4.4 Dispersion Analysis

At the beginning of this chapter a dispersion plot was shown along with a typical power spectra plot in Figure 4.1. This was for the purpose of doing a simple discussion of on some of the benefits of using a dispersion analysis on optical wavefronts. That simple analysis was using only a single row of a wavefront and provided an incite into the disturbances that were moving in the horizontal direction only. When a dispersion analysis is performed over all dimensions of a wavefront, as will be done for the remained of the chapter additional detail is available, additional detail as well as determination of optical disturbances moving vertically or any direction in between. Figure 4.2 shows a comparison between the two-dimensional single row dispersion and a three-dimensional dispersion showing the just the horizontal moving optical disturbances at both zero-vertical spatial frequency and the maximum value through all vertical spatial frequencies. The top plots shows the two-dimensional dispersion plot that was previously shown in Figure 4.1 but this time with a linear temporal frequency axis. The middle plot shows the three-dimensional dispersion plot at $\xi_y = 0\ m^{-1}$, which shows a significant amount of additional data. The two-dimensional dispersion shows a wide swath of signal that is generally traveling upstream from a line that goes through the origin and has a slight amount of positive slope downward to a line with a significant amount of negative slope. This discussion of slopes is of the relative visible slope in the plots due and not actual slope calculation as the temporal frequency axis is several orders of magnitude larger than the spatial frequency axes (footnote?).

The slice of the full three-dimensional dispersion shows signal at the same limits for the two-dimensional swath of signal with some signal laying along the temporal frequency axis at $\xi_y = 0\, m^{-1}$. This signal represents a collection of stationary modes at each temporal frequency. If this were to be some flow related phenomenon the velocity the disturbance would be nearing infinity. On the three-dimensional dispersion plot there are easily observable signals that run parallel to the strongest signals but do not emanate from the origin. These are signals that have been aliased due to the sample rate, either spatial or temporal, being to low. This has some interesting implications in the possibility of being able to artificially increase the sample rate as will be discussed later.

The bottom plot of Figure 4.2 shows the maximum value at each $f - \xi_x$ location through the range of ξ_y values. This effectively recreates the two-dimensional dispersion plot is a higher signal to noise ratio. The aliased data is far more noticeable in this plot an in the two-dimensional one. This indicates that a two-dimensional dispersion analysis is approximately the maximum value of the three-dimensional dispersion in a given dimension. A reduced order dispersion can be calculated by

$$S_{xx}^{n-1} = \max(S_{xx}^{n}, m) \cdot f_s^m, \tag{4.16}$$

where S_{xx}^n is the n-dimensional dispersion, $\max(x, m)$ is the maximum value of x in the m-th dimension, and f_s^m is the sample rate in the m-th dimension. This can be shown in Figure 4.3. The recovered power spectra from the two-dimensional dispersion analysis is a good estimation at the center of the frequency range but has some diversion near the edges. It stays within half an order

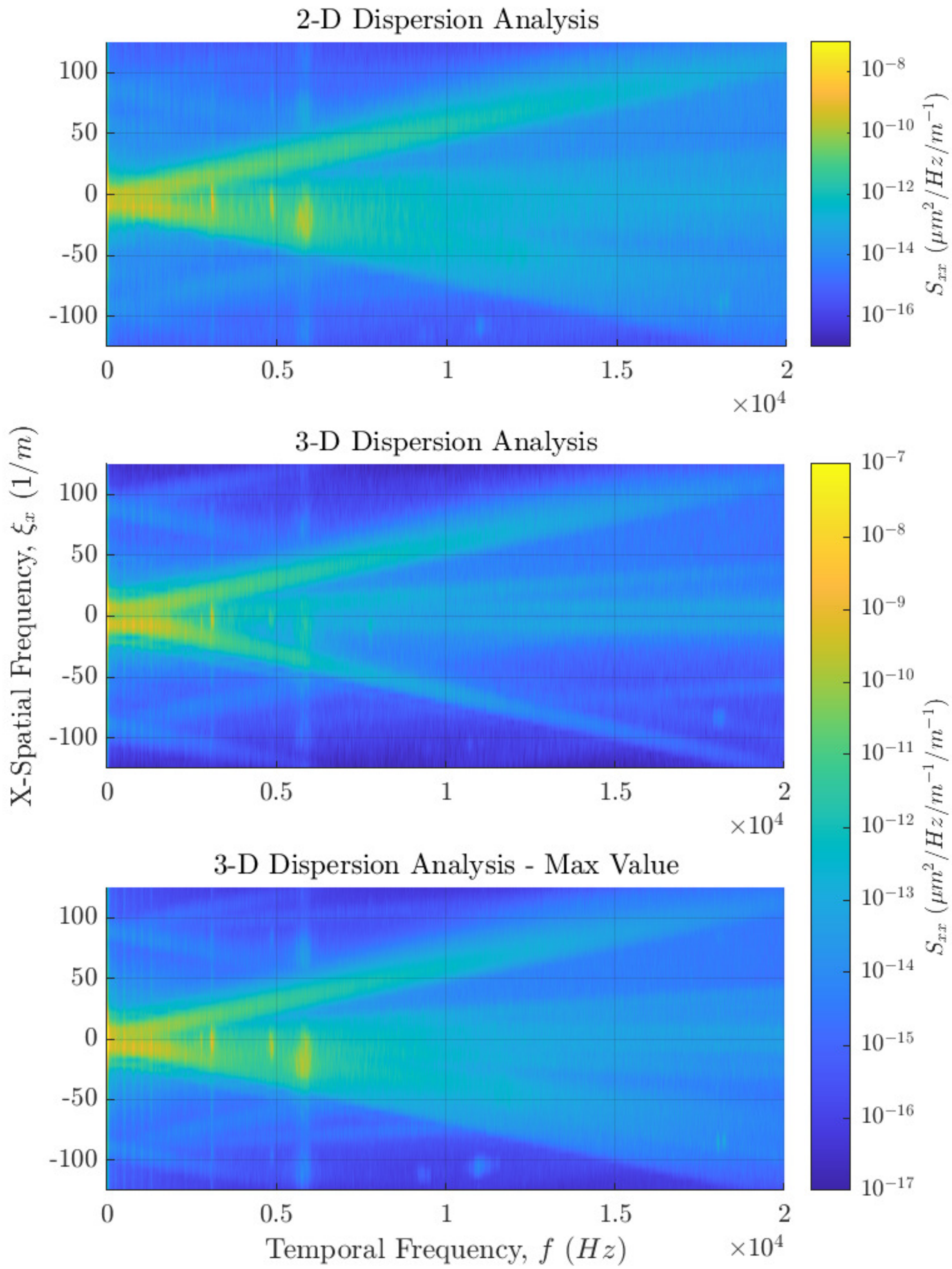

Figure 4.2. Horizontal moving optical disturbances comparison. The top plot shows a two-dimensional dispersion analysis over a single row of data. The middle plot shows a three-dimensional dispersion analysis at $\xi_y = 0$. The bottom plot shows the same three-dimensional dispersion analysis but showing the maximum value through the vertical axis.

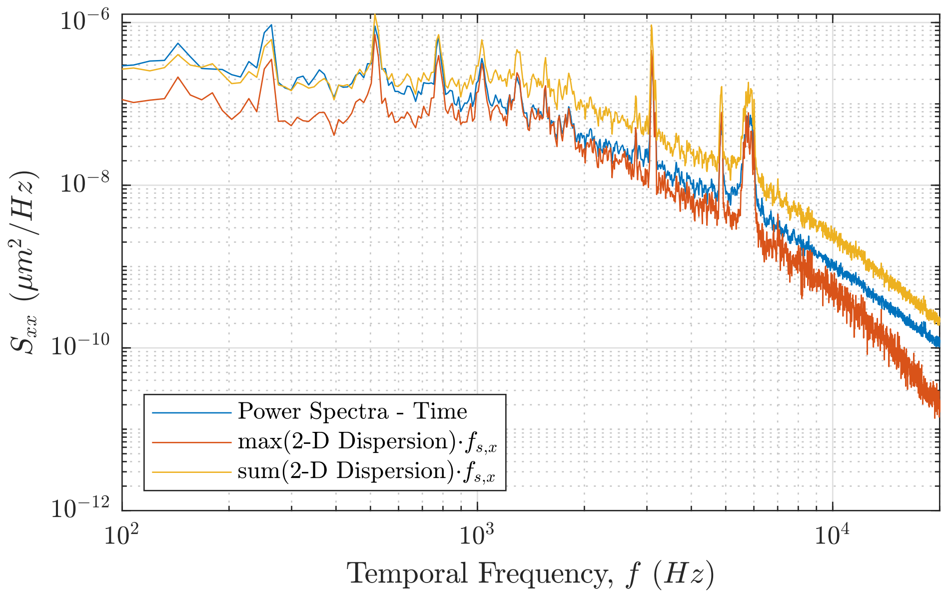

Figure 4.3. Recovery of time-based power spectra from two-dimensional dispersion analysis.

of magnitude below 1000-Hz with the signal peaks being a much closer approximation. On the high end, the recovered power spectra has a decay rate that runs even with the direct computation up to about 10,000-Hz at which point the decay rate increases.

4.4.1 2-D Slices of Full Dispersion

The full dispersion analysis contains information of flow features not only moving in the horizontal direction as the two-dimensional dispersion showed but also in the vertical direction and the combinations of the two. Figure 4.4 shows slices of the full dispersion in both the horizontal and vertical directions along with lines representing critical velocities. Each of these plots is shown when the other spatial frequency is equal to zero, meaning that the disturbances shown are moving solely in that direction.

The top plot shows the horizontally moving optical disturbances that has been shown previously. There are three major flow related structures that can be observed. The top most flow related structure is the boundary layers on both sides of the wind tunnel. It can be seen that the boundary signal has a sharp drop off at the free-stream velocity, u, and has a slight decay as the velocity decreases (increasing slope). Figure 4.5 shows the boundary layer velocity at a few cuts a little more clearly. The boundary layer velocity has typically be reported as approximately $0.83u$ [14].

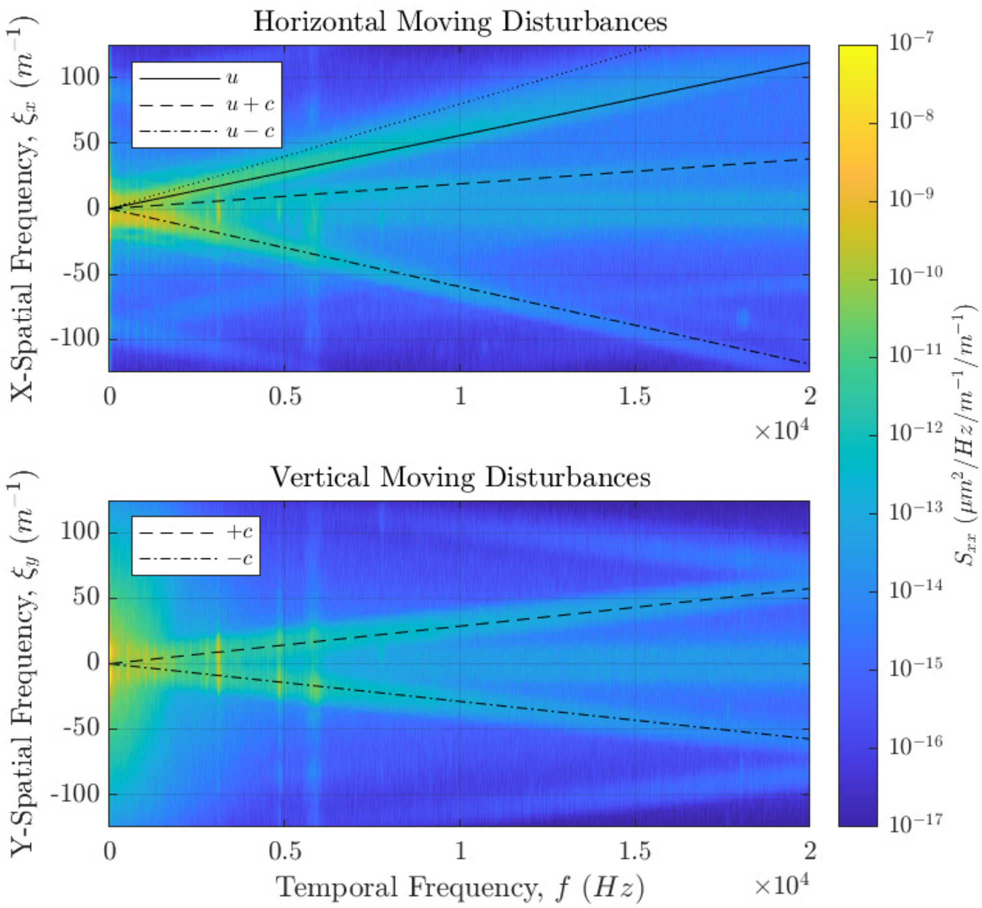

Figure 4.4. Horizontal and vertical moving optical disturbances. This is the same data as presented in Figure 4.1 but after calculating the full three-dimensional power spectra. The horizontal disturbances are shown at zero vertical spatial frequency and likewise the vertical disturbances are shown at zero horizontal spatial frequency.

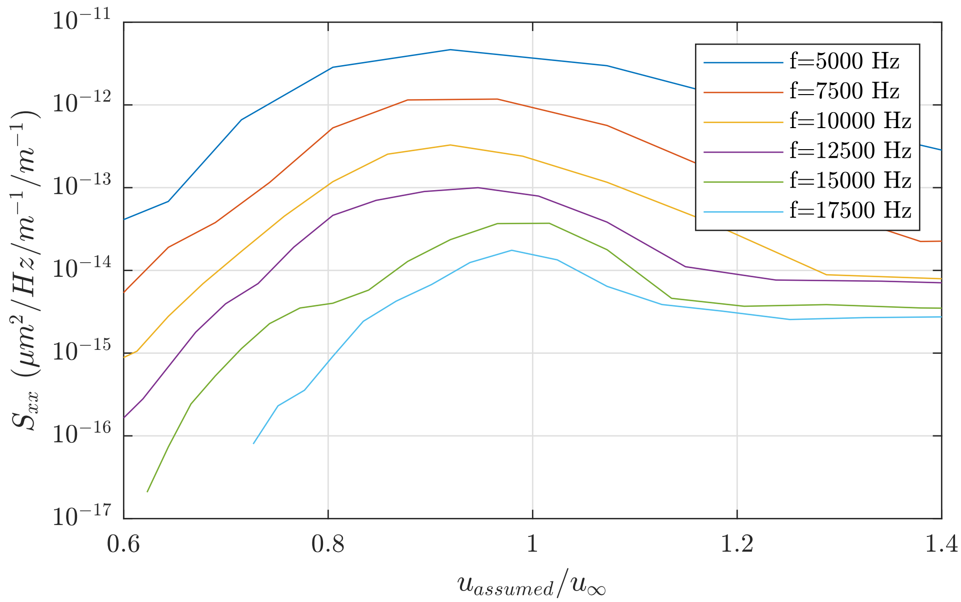

Figure 4.5. Assumed boundary speed at various temporal frequencies.

This data shows the boundary layer velocity has a range of velocities at each given frequency in which the peak velocity component has some dependence on the temporal frequency. The lower frequencies tend to have a lower velocity of around $0.9u$ which is higher than has typically been reported while the higher frequencies approach the free-stream velocity. When placing a lower bounding line on the boundary layer line in terms of speed in Figure 4.4, a value of approximately $0.7u$ seems to do a good job at bounding most of the boundary layer signal along with the free-stream velocity line.

The next two major flow related structures deal with acoustic signals traveling in both directions through the wind-tunnel. The downstream traveling acoustic wave, $u + c$, typically has a low signal strength than the upstream traveling acoustic wave, $u - c$, due to the downstream traveling wave having a longer wavelength and thus more signal being filtered out due to aperture filtering [36]. At the low frequencies, the blade-passing frequency and its associated harmonics can be seen with regular spacing. There also appears to be some constructive interference with the BPF and some of the aliased data around $\xi_x = \pm 100\ m^{-1}$.

In both the horizontal and vertical moving plots the stationary modes are a prominent feature. The two main features on the vertical moving disturbance plot is the signal at the speed of sound as well as some significant aliasing. These to lines represent acoustic waves that are traversing either straight up or down. Some of the high frequency spikes (3, 5, and 6-kHz) seems to be laying along these speed of sound lines in the vertical direction and stationary in the horizontal direction. These spikes maybe something in the test-section itself, along the top and bottom walls that is being excited and resonating.

4.4.2 3-D Representations of Full Dispersion

While the two-dimensional slices are fairly informative, particularly when it comes to signal strength of various flow structures and their velocities, a three-dimensional plot allows better visualization of the overall flow structures but some details are lost. The same data that has been previously shown in slice form, is depicted in Figure 4.6 as an isosurface with a power of 10^{-14} $\mu m^2/Hz/m^{-1}/m^{-1}$ and shown from four different views. This particular isosurface encompasses approximately 99.9% of the power of the optical disturbances with little aliased information represented. The largest feature is the boundary layer which resembles an ellipsoid or elliptical wing. The other main feature is the acoustic signal which appears as a cone which has been tilted over a little bit. The acoustic signal has several predominate spikes which form at high temporal frequencies indicating that there may be a small number of dominate duct modes. The last feature is the stationary modes which have a near constant shape and magnitude through all frequency ranges.

Figure 4.7 shows two views of this three-dimensional dispersion but over a range of Mach numbers. All of these plots are of an isosurface with the same strength as used in Figure 4.6. For a Mach number of 0.3, top plot, the most noticeable feature is the stationary modes which do not seem to change much as the Mach number is increase. This indicates that the stationary waves are mostly as measurement artifact that could be from either laser or camera noise. The boundary layer signal increases in power significantly as Mach number is increased but also the slope is significantly increased as well. The acoustic signal sees some interesting evolution as well. Along with the strength greatly increasing with Mach number, the slope of the upstream traveling disturbances decreases significantly while the downstream moving acoustic disturbances do not see much change other than an increase in signal strength.

While the three-dimensional views offer some significant incite, sometimes the insides need a close look a shown in Figure 4.8. This figure shows slices of the dispersion array at several different temporal frequencies: a mean lensing slice at 0-Hz, the blade-passing frequency at 517-Hz, the second harmonic of the blade-passing frequency at 1551-Hz, and additional slices at 5, 10, and 20-kHz. The mean lensing slice at 0-Hz shows a mostly axisymmetric pattern that is strongest in the center and dies out as the distance from the origin increases. There appear to be the occasional spike radiating out from the center, most noticeably in line with the boundary layer signal.

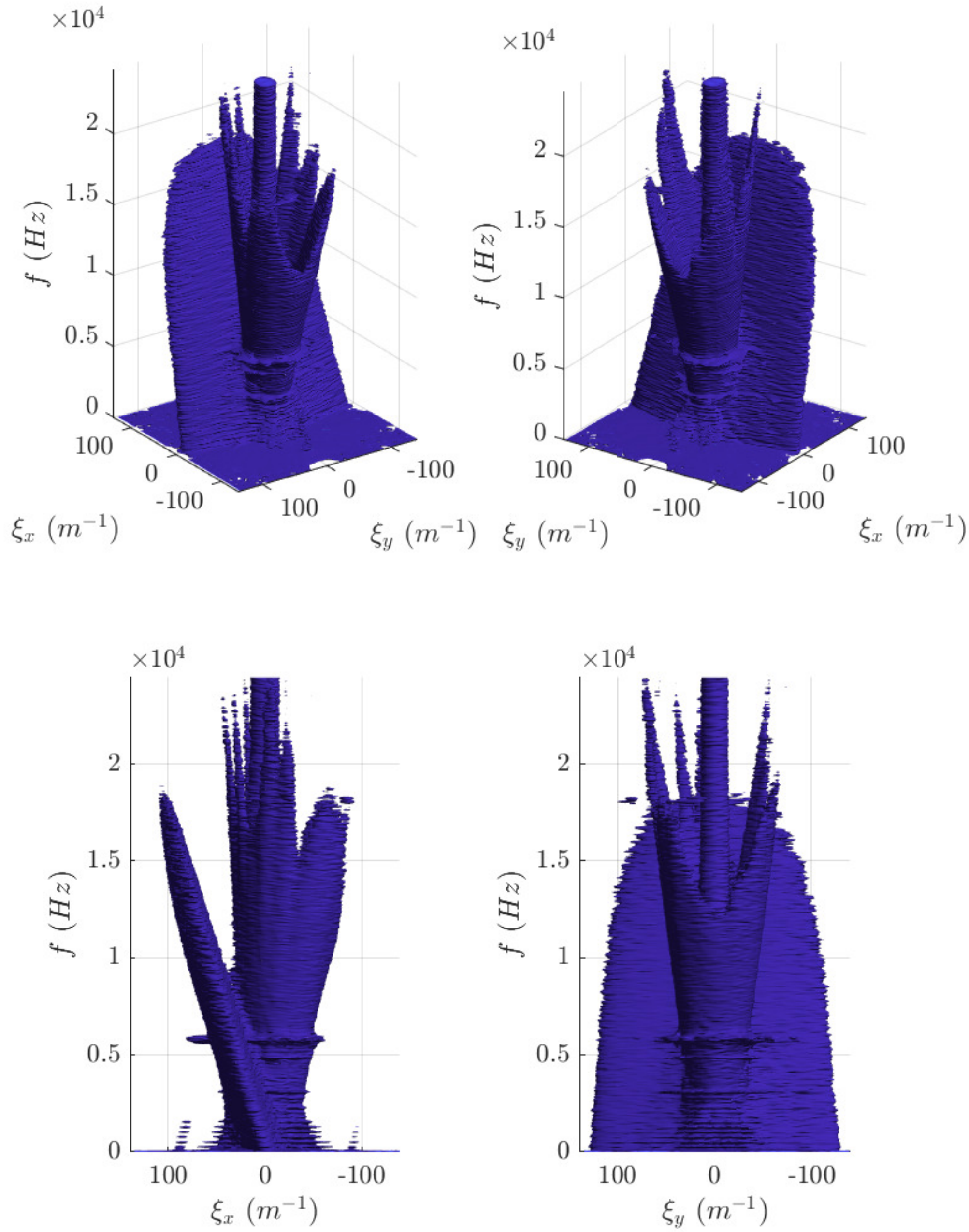

Figure 4.6. Three-dimensional view of the dispersion plot showing an isosurface at a power of 10^{-14} $\mu m^2/Hz/m^{-1}/m^{-1}$. The isosurface encompasses 99.9% of the power of the wavefront.

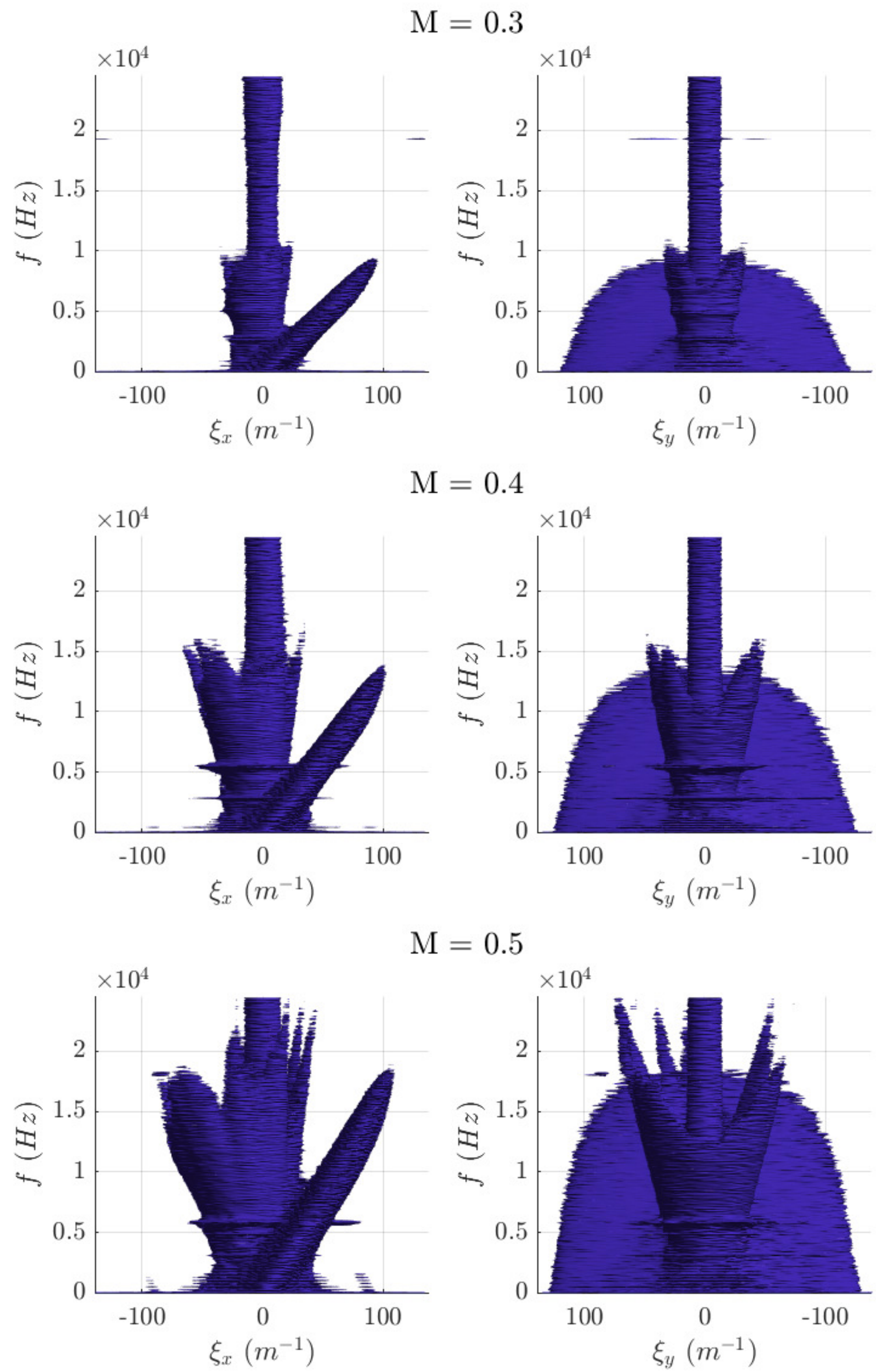

Figure 4.7. Three-dimensional view of dispersion plots as the Mach number increased from 0.3 to 0.5. The isosurfaces are all shown at a power of 10^{-14} $\mu m^2/Hz/m^{-1}/m^{-1}$ and all encompass 99.9% of the wavefront power.

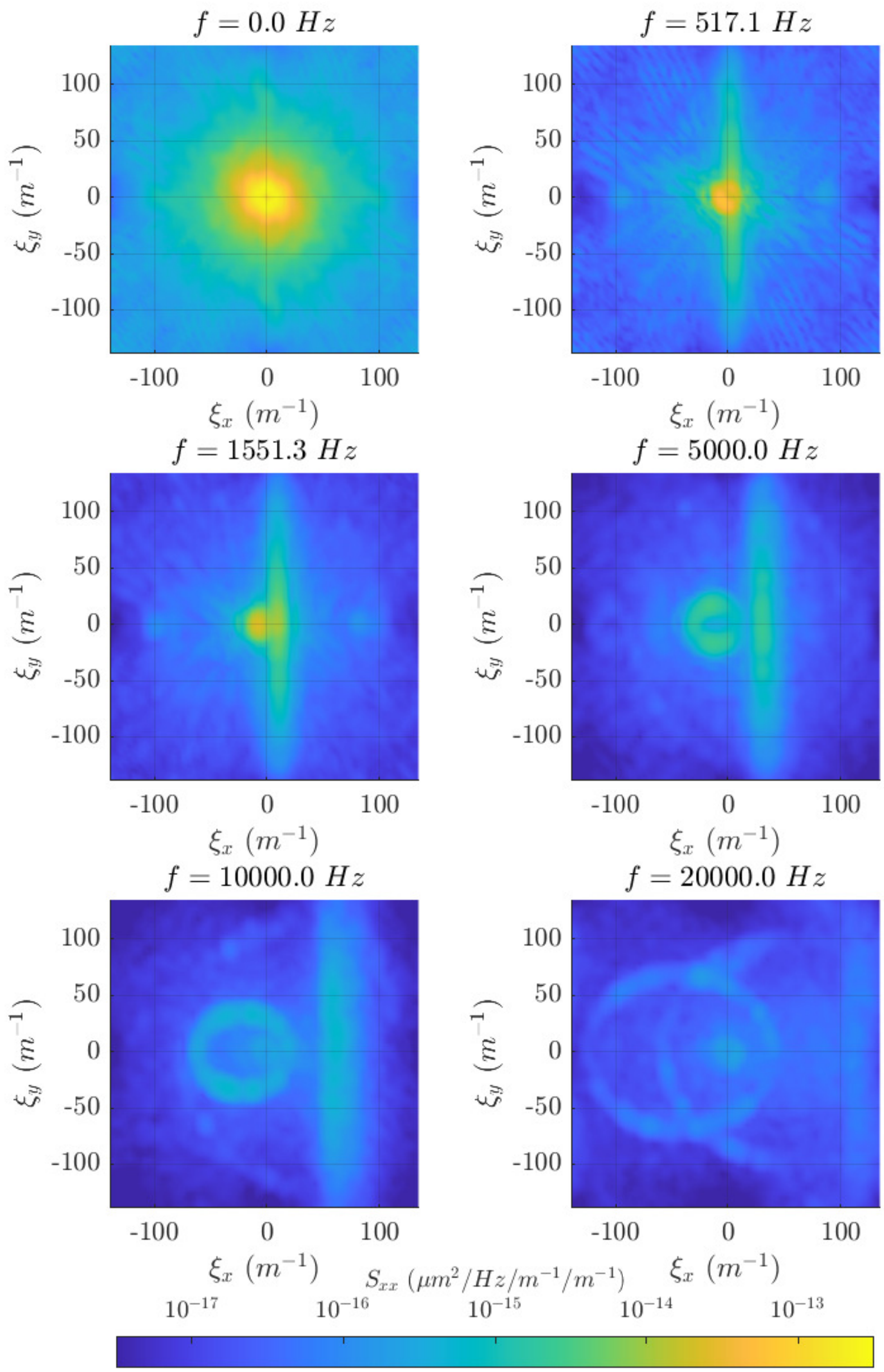

Figure 4.8. Additional dispersion slices at various temporal frequencies.

The next four slices show boundary layers structure slowly moving towards positive x-spatial frequencies. It does appear to be rotated slightly counter-clockwise indicating that the interrogation beam is slightly rotated between the test section and the wavefront sensor. The boundary layers signal at the lower frequencies appears to be more elliptically shaped while the higher frequencies appear to have a sharp drop in signal strength going towards the origin and are slightly more feathered going away. This could be indicative of lower frequency disturbances in the boundary layer typically traveling at a more uniform speed very near the free-stream velocity likely being either in the outer boundary layer or free-stream tunnel turbulence. The higher frequency disturbances seem to have a wide range of velocities that approach the free-stream velocity and are likely small structures that span some significant portion of the boundary layer.

The acoustic disturbances show an interesting evolution as the frequency increase from fairly compact and strong signal just on the upstream traveling side of things around the blade-passing frequency to elliptical shaped rings at the higher frequencies. At 20-kHz, there are two elliptical shapes that are easily identifiable, the smaller one is the signal that is actually present at that frequency while the other one is some aliased data due to a limited temporal sample rate. The 10-kHz slice shows a little bit of acoustic aliasing Both the 10 and 20-kHz acoustic rings show some favorable spatial frequencies which could also be seen in the three-dimensional view as spikes. These two slices also show the center stationary modes that appear to be nearly identical.

4.4.3 Artificially Increased Sample Rate

Aliased data has been partially discussed previously. When a signal crosses a plane represented by one of the Nyquist frequencies (positive or negative) it transposed to the conjugate Nyquist frequency plane and continues on with the same gradient as before, which is shown in Figure 4.9 using the horizontal and vertical dispersion slices. Here the black box represents the original dispersion plot, while outside of that box is data that has an artificially increased sample rate. This process can be accomplished by simply tiling the entire dispersion array in the desired dimension. In this case the dispersion array was tiled in a three-by-three grid for each of the horizontal and vertical slices. Along the spatial Nyquist frequency edges, there is a significant dip in the signal strength which would result in a spatial super sampling to have a significant loss of signal at these frequencies.

On the upstream moving disturbance side there is some noticeable aliasing that is present including a significant spike at 18-kHz (-80-m^{-1}) while aliased and about 31-kHz (-200-m^{-1}) when it

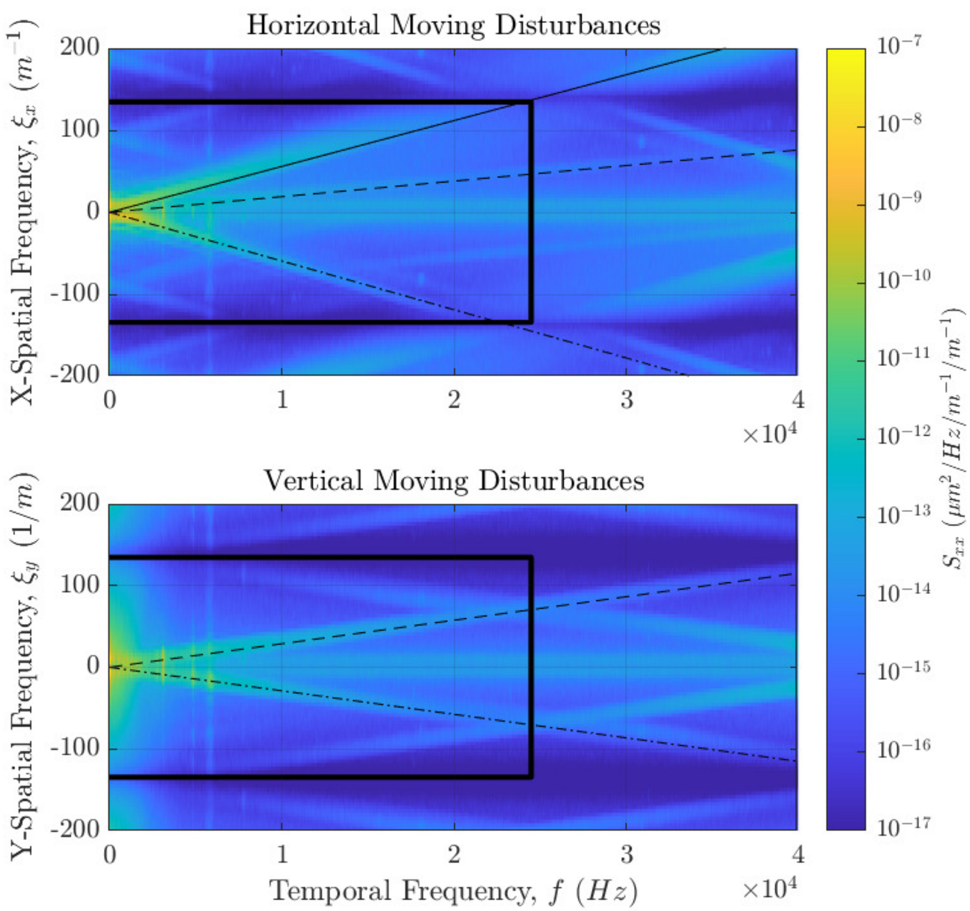

Figure 4.9. Artificially increased temporal sample rate using a dispersion analysis. The black box represents original dispersion plot.

has been unaliased. As that upstream moving acoustic disturbance crosses the spatial Nyquist frequency, the signal strength drops significantly to local background levels. The boundary layer signal is unfortunately to well aligned with its tiled self for any aliased data to be noticeable. The vertically moving disturbances have some significant temporal aliasing but little to no spatial aliasing.

Just as the aliased signal is unaliased into the higher frequencies, non-aliased data is aliased into higher frequencies. This means that some sort of filtering technique will need to be employed. These filters should not only be designed to remove the aliased data from actual sample but also the aliased data from the super sampled frequencies.

CHAPTER 5

SYNTHETIC WAVEFRONT

In order to best understand how some basic filters preform on a set of data, a fully known synthetic wavefront was generated such that all of the various components could be generated separately with the combined product filtered and compared to the synthetic wavefront containing only relevant aero-optical data. This is done by creating an input dispersion plot where each source component is separately generated with parameters that can be modified to alter the output signal as necessary. Signals that are assumed to be statistically independent are converted into dimensional space separately and then summed together. While signals that are assumed to be related to one another (such as the sound and vibration components) are summed together in frequency space. Figure 5.1 shows the input dispersion plot with each signal component separately colored. The aero-optical signal is shown in red, the stationary modes in blue, duct acoustics in magenta, blade-passing frequency related corruption in green, slowly varying mean-lensing in yellow, and background in cyan.

Wavefronts were generated to approximate the sample conditions in that the data presented in Figure 4.6 were measured with. The sample rate was 200 m^{-1} with 64 (2^6) samples in the spatial dimensions and 30,000 Hz with 8192 (2^{13}) samples in the temporal dimension. The speed of sound was chosen to be 340 m/s, with a Mach number of 0.6, and a boundary layer velocity of 163.2 m/s ($0.8U_\infty$).

The general process of developing most of the component signals was to determine an approximate shape, normalize it in the appropriate dimensions, and scale the result by using a function derived from a hyperbola,

$$\frac{\log_{10}(WF) - b}{b^2} - \frac{\xi_{\rho_N}^2}{a^2} = 1, \tag{5.1}$$

such that the signal strength at unity of the normalized radial frequency, $\log_{10}(WF(\xi_{\rho_N} = 1))$, and the limiting slope, a/b, are inputs. This results in the signal strength of the wavefront being

$$\log_{10}(WF) = b - \sqrt{\frac{\xi_{\rho_N}^2}{m^2} + b^2}, \tag{5.2}$$

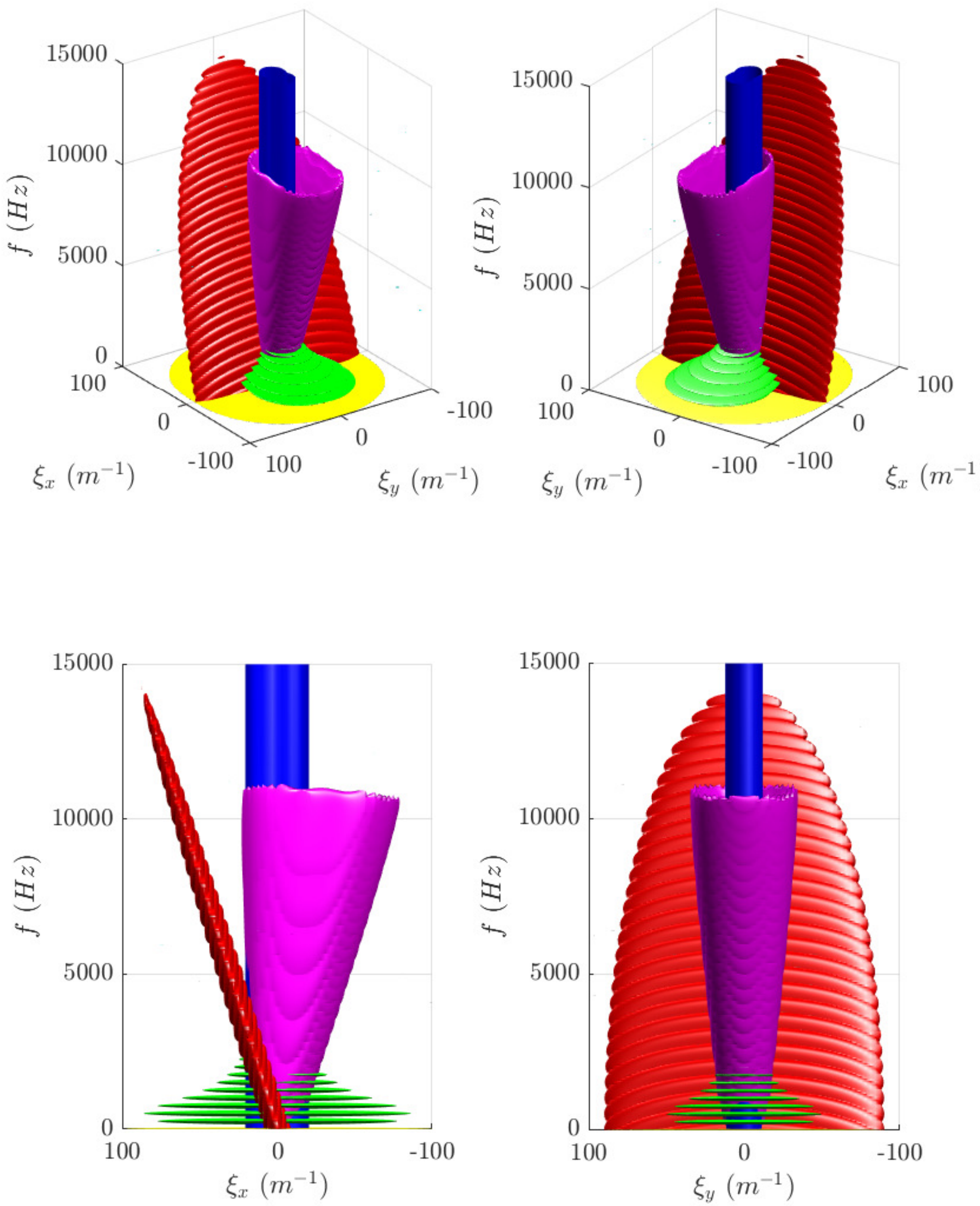

Figure 5.1. Synthetic wavefront input dispersion plot of an aero-optical signal and various signal corruption components. The aero-optical signal is shown in red, the stationary modes in blue, duct acoustics in magenta, blade-passing frequency related corruption in green, slowly varying mean-lensing in yellow, and background in cyan.

where

$$b = \frac{1}{2\log_{10}(WF(\xi_{\rho_N}=1))} \cdot \left(\log_{10}(WF(\xi_{\rho_N}=1))^2 - \frac{1}{m^2} \right). \tag{5.3}$$

The code used to generate the synthetic wavefront used in this section is shown in Listing A.3.

5.1 Aero-Optical Signal

The aero-optical signal which is approximating an optical beam passing through a boundary layers normal to each of the test section walls. This signal was approximated by creating an ellipsoid in the plane of the feature's velocity and normalizing the radius by some arbitrary factors to roughly match the shape of the measured dispersion plot shown in Figure 4.6. The dispersion magnitude was then calculated by applying Equation 5.2, with relevant code shown on Lines 19-30 of Listing A.3. In Figure 5.1 the aero-optical signal is shown in red.

5.2 Stationary Mode Signals

The stationary modes in Figure 4.6 appear to be temporally white-noise with the spatial frequencies forming an epicycloid of $k = 2$. This shape was further simplified using a single trigonometric function to represent the normalization function of the radial spatial frequency,

$$\xi_{\rho_N} = \frac{\xi_\rho}{\xi_{\rho_0}\sqrt{10 - 6\cos(2\xi_\theta)}}, \tag{5.4}$$

this makes an epicycloidal like shape which has a smooth derivative. This dispersion component is shown in blue in Figure 5.1 and the relevant code shown in Lines 61-66 of Listing A.3.

5.3 Sound & Vibration Signals

The sound & vibrating component signals are comprised of two parts. The first of these is the blade-passing frequency and its harmonic disturbances (shown in green in Figure 5.1) and the second is the acoustic duct modes (shown in magenta). Like the stationary modes, the blade-passing frequency disturbances were modeled with the simplified epicycloid narrow-band disc and each harmonic was modulated by using a low-pass filter offset to the blade-passing frequency. The code for the blade-passing frequency disturbances is shown in Lines 97-113 of Listing A.3.

The acoustic duct mode disturbances form a cone which in the $f - \xi_x$ plane is defined by the lines $u \pm c$, while in the $f - \xi_y$ plane is defined by the speed of sound. At each temporal frequency step an ellipse was defined based on the constraining lines and the distance to that ellipse used to calculate a normalized radial frequency. The strength of the disturbance was decreased logarithmically in temporal frequency as shown in the code in Lines 183-200 of Listing A.3.

5.4 Mean Lensing Signal

The mean-lensing signal (shown in yellow in Figure 5.1) uses a stretched version of the simplified epicycloid and represents the slowly varying spatial disturbance. The relevant code is shown on Lines 144-152 of Listing A.3.

5.5 Background Noise Signal

The background noise disturbance (with a few small spots shown in cyan in Figure 5.1) was the only component that did not use the hyperbola to scale the signal but instead was just normally distributed random noise with a mean noise level and deviation as inputs. The relevant code is shown in Lines 230-234 of Listing A.3.

5.6 Synthetic Wavefront Creation

A synthetic signal can be created from a power spectra by solving for x in Equation **??** and using the Inverse Fast Fourier Transform,

$$x(t) = \mathrm{REAL}\left[\mathrm{IFFT}\left\{\sqrt{S_{xx} \cdot N \cdot f_{samp}} \cdot \exp i\phi\right\}\right], \tag{5.5}$$

where REAL is the real component and ϕ is a random set of phases for each point in the measurement space. As shown previously this relation can be extended into n-dimensions,

$$f(\mathbf{x}) = \mathrm{REAL}\left[\mathrm{IFFT_n}\left\{\sqrt{\mathbf{S_{xx}} \cdot \prod \overrightarrow{N} \cdot \overrightarrow{f}_{samp}} \cdot \exp i\phi\right\}\right]. \tag{5.6}$$

Care should be taken when constructing the random set of phases, as the zero-frequency component has zero phase and the phases on either side of it are conjugates of one another. The code for creating a wavefront from a dispersion plot is shown in Lines 336-340 of Listing A.3 and is specifically creating the wavefront for the aero-optical signal but other signals are generated using the same basic code. Note that the first three lines are to get the set of phases properly configured that creates conjugate phases rotated about the origin.

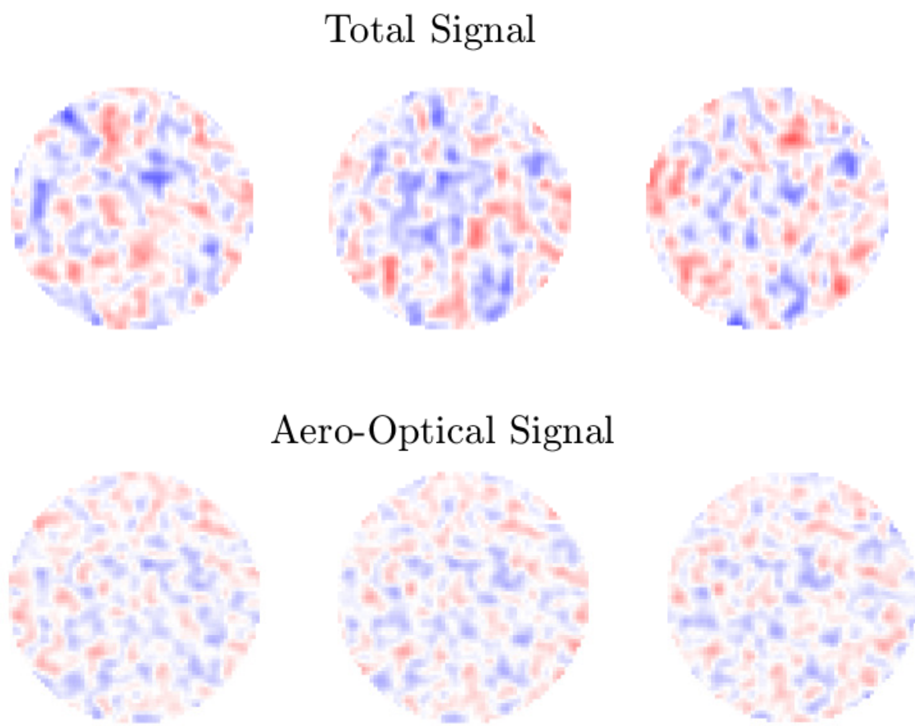

Figure 5.2. Sample frames from the synthetic wavefront with the total wavefront signal on top and the aero-optical only signal bottom. Flow is from right to left.

It was assumed that the aero-optical signal, the stationary modes, and the background noise were statistically independent of one another and the sound and vibration combination of modes and as such could be separately transformed into physical space. While the components of the sound and vibration sources, the blade-passing frequency, the acoustic cone, and the mean-lensing, were assumed to be related to one another and thus were summed together in frequency space prior to being transformed into physical space. Once the separate components were in physical space the total wavefront was obtained by summing up the separate components with the aero-optical signal being a separately saved along side the total wavefront. Some frames from the synthetic wavefront are shown in Figure 5.2 with the total wavefront shown on top and the aero-optical only signal shown on the bottom. Flow is from right to left. The aero-optical signal is often times noticeable in the total wavefront signal, but can be easily overpowered by the various contamination sources.

5.7 Comparison to Measured Data

A dispersion plot of the total synthetic wavefront is shown in Figure 5.3. In this view the aero-optical signal is more noticeable but there still remains some significant overlap with the various contamination sources. While the mean-lensing component is not as visible in this isosurface, the rest of the dispersion plot in a good representation of the input dispersion plot shown in Figure 5.1. The blade-passing frequency was depicted as symmetric in the synthetic wavefront while measured data (shown in Figure 4.6) shows more signal on the side traveling in the direction of flow. The harmonics of the BPF are more on the upstream traveling side of the dispersion and are a little less pronounced in the measured data. The total synthetic wavefront has a spatial time-averaged RMS of $0.0112 \pm 0.0006\mu m$ with the aero-optical only signal having a spatial time-averaged RMS of $0.0073 \pm 0.0003\mu m$. The measured wavefront presented in Figure 4.6 had a spatial time-averaged RMS of $0.0874 \pm 0.0263\mu m$. The overall spatial RMS of the synthetic wavefront was 12.8% when compared to the measured wavefront indicating that the algorithms used to generate the wavefront are not representative of reality and can provide a future path of research in order to produce more realistic synthetic wavefronts. Double Check line numbers for the Listings.

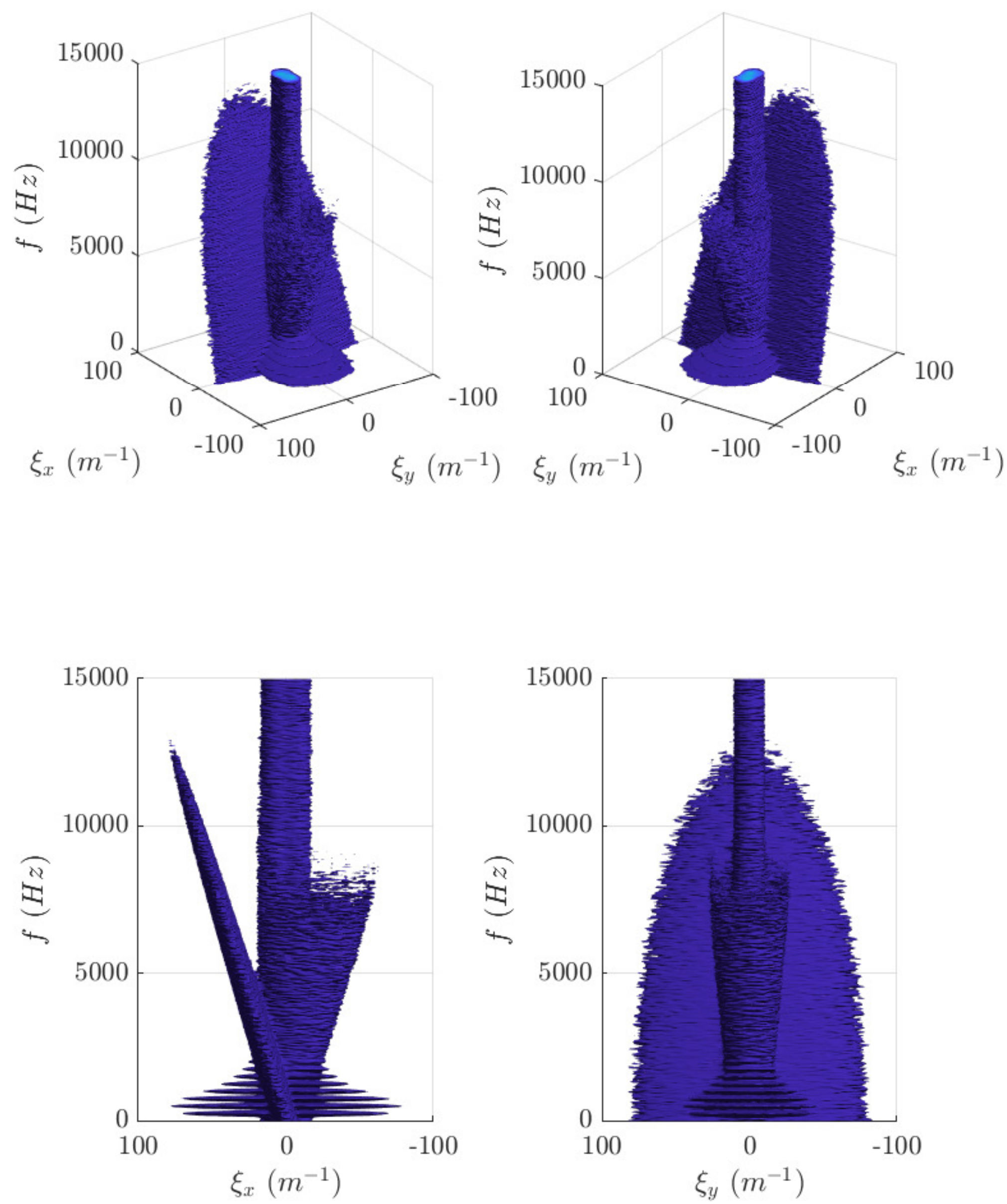

Figure 5.3. Synthetic wavefront output dispersion plot of an aero-optical signal and various signal corruption components.

CHAPTER 6

SINGLE SENSOR FILTERING TECHNIQUES

Show some dispersions of POD modes and discuss whether or not POD filtering maybe a viable option.

A filter is a function, $G(\omega)$, that describes the gain a signal will experience in frequency space. In the simplest case, the filtered signal is the inverse Fourier transform of the gain multiplied by the Fourier transform of the signal. Additionally, a windowing function, $W(\mathbf{x})$, can be used to help suppress finite sampling effects,

$$f_F(\mathbf{x}) = \mathrm{REAL}\left(\frac{\mathrm{IFFT_n}[G(\omega)\cdot \mathrm{FFT_n}\{f(\mathbf{x})\cdot W(\mathbf{x})\}]}{W(\mathbf{x})}\right), \tag{6.1}$$

where f is the signal function and f_F is the filtered signal. Depending on the windowing function some data could be destroyed during this process if there is a zero present due to the possibility of dividing by zero.

A basic MATLAB code for applying a filter to a wavefront using a separate function for both generating and applying the gain function which is presented in Listing A.4. This code generates a windowing function as described by Equations 4.5, 4.12, and 4.15. The temporal windowing function was generated with an additional two terms such that the end points which are equal to zero could be removed to prevent the first and last frames from being destroyed. Likewise, the spatial window used the arbitrary aperture function which ensures that all of the points inside of the aperture are non-zero. In some cases, a windowing function was not used due to filtered wavefront having a far greater magnitude in some places despite the precautions used. The filter presented in this code sample is a second order temporal high-pass filter with a cut-off frequency of 2000 Hz. The function WFfilter takes input based on a normalized cut-point in reference to the sample rate.

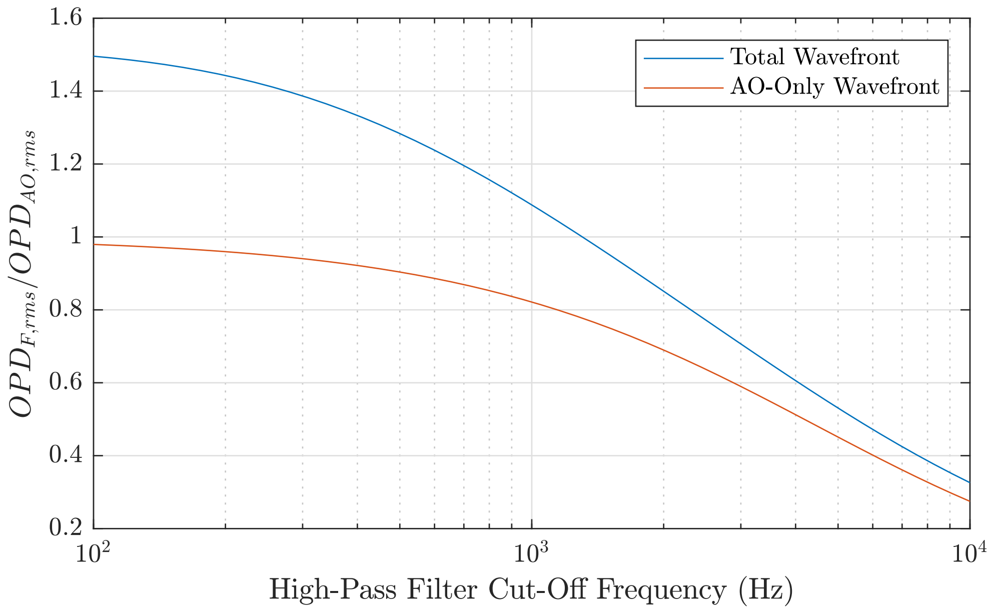

Figure 6.1. OPD time-averaged spatial-RMS of high-pass temporal filters relative to the aero-optical only unfiltered wavefront.

6.1 Temporal Filter Methods

The methods presented in this section are based on Butterworth filters [5] but could easily be extended to other types of filters. The basic gain function,

$$G(f) = \frac{1}{\sqrt{1 + \left(\frac{f}{f_c}\right)^{\pm 2n}}}, \tag{6.2}$$

where f_c is the cut-off frequency, n is the filter order (number of filters in a series), and $\pm$ represents either a low-pass $(+)$ or high-pass $(-)$ filter. In this particular formulation, only the magnitude is attenuated, circuit based Butterworth filters or their digital copies will have some variable phase attenuation as well. Additionally, a band-pass filter can be constructed by placing a low-pass in series with a high-pass filter and a band-stop by placing the two types in parallel.

As a large portion of the wavefront contamination is at low frequencies, a high-pass filter is the most useful in temporal space for removing unwanted contamination, as shown in Figure 6.1. This figure shows the time-averaged spatial-RMS of both the total and aero-optical only wavefronts with various cut-off high-pass filters relative to that of the aero-optical only wavefront unfiltered. The total wavefront ratio crosses unity around 1200 Hz, which is about halfway between the second and third harmonic of the blade-passing frequency in this simulated wavefront. While approximately 75% of the aero-optical signal remains at this cut-off frequency, that difference is made up by the remaining contamination. This can provide a computationally cheap way estimating the aero-optical portion of the wavefront for calculations that rely on the spatial-RMS of a wavefront. While it is easy to determine a cut-off frequency for this synthetic wavefront, a measured wavefront will likely take some knowledge or expectation of the contamination that is present in the measurement.

An example of band-pass and band-stop filtering is shown if Figure 6.2. The figure shows measured data that is band-stop filtered in the left column and band-pass filtered in the right column in several different frames. The flow is from right-to-left and the band-pass filtered wavefront clearly shows upstream-moving optical disturbances associated with acoustic duct modes traveling upstream from the fan. The band-stop shows a much slower moving optical disturbance that is in general moving in the direction of the flow, but it still possess the optical disturbances of the blade-pass frequency harmonics.

One thing of note, MATLAB's builtin filter functions only work in one-dimension of frequency space and are unable to determine the direction that a signal is traveling. They also only apply the filter to the positive frequencies and zero-out the negative ones which both reduces the signal by two and also switches all disturbances to moving in the same direction. So even for a filter that operates in one-dimension, it is best to apply the filter over both positive and negative frequencies to the n-dimensional Fourier transform in order to preserve the direction of travel of a signal. This additionally allows several filters to be applied in series with one another without having to perform a Fourier and inverse Fourier transform for each successive filter. I should maybe show this matlab filter issue in an appendix.

Some additional uses of temporal filters would be in sizing and/or designing an adaptive optics system. A low-pass filter with a cut-off at the bandwidth of either a fast-steering or deformable mirror would help determine the signal that a system would need to reject. A control system may need to have the bandwidth reduced in order to keep a mirror's travel within limits. While a high-pass filter would inform designers of the remaining optical aberrations that cannot be corrected.

6.2 Upstream/Downstream Moving

For the filtering of upstream and downstream moving optical disturbances a logistic function was chosen,

$$f(x) = \frac{1}{1 + \exp\{-kx\}}. \tag{6.3}$$

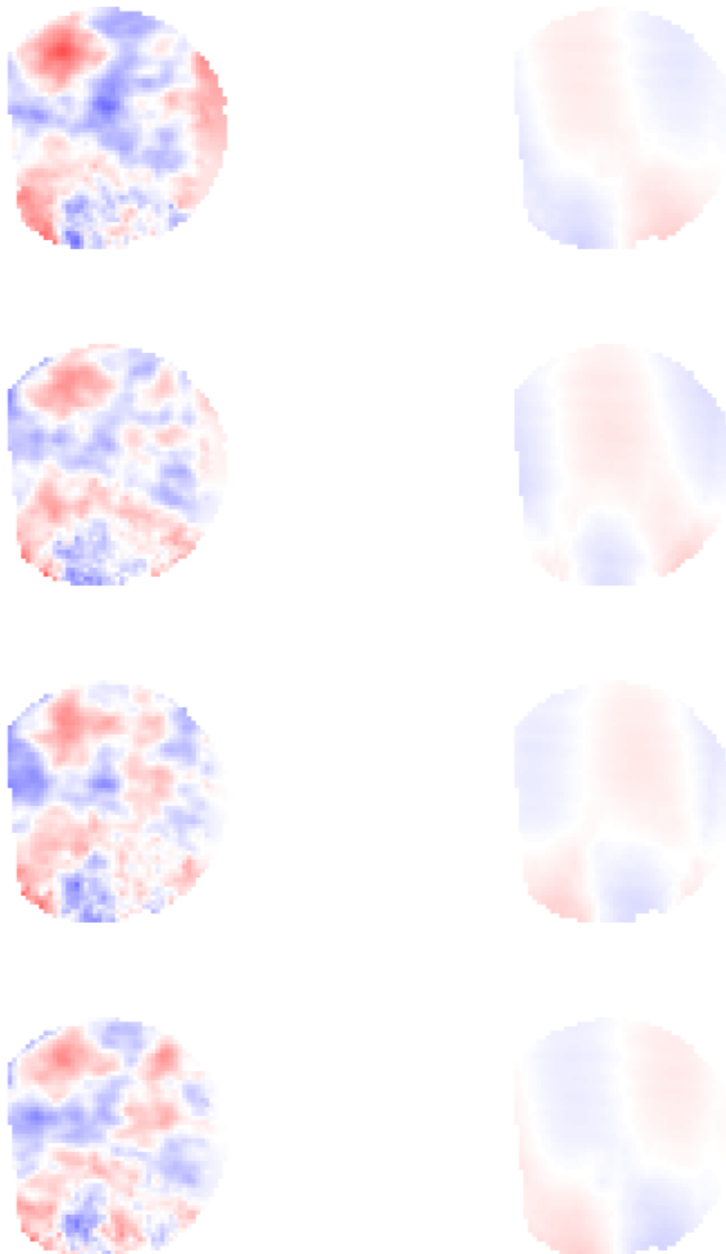

Figure 6.2. Measured wavefronts filtered at the blade-passing frequency (532±10 Hz). The left column is band-stop filtered while the right is band-pass filtered.

This function needs to be expanded into two-dimensions (x and t) with the filter ideally returning a value of one in both the first and third quadrants and zero otherwise for a filter outputs disturbances moving in the direction of flow. To accomplish this the logistic curve in each dimension is scaled and offset to output values between negative one and positive one,

$$G_t(f) = \frac{2}{1 + \exp\{-k_t f\}} - 1 \tag{6.4}$$

and

$$G_x(\xi_x) = \frac{2}{1 + \exp\{\pm k_x \xi_x\}} - 1, \tag{6.5}$$

where $\pm$ determines whether the filter is obtaining upstream traveling disturbances $(+)$ or downstream traveling $(-)$. These two gain functions are then multiplied together and scaled to output values between zero and one,

$$G(\xi_x, f) = \frac{(G_t \cdot G_x) + 1}{2}. \tag{6.6}$$

As the values of k_x and k_t go to infinity an ideal case is obtained. Downstream traveling disturbances have a gain of one in the first and third quadrants, zero in the second and forth quadrants, and a value of 1/2 when either frequency is zero.

The dispersion analysis using an ideal downstream moving filter on the synthetic wavefront is shown in Figure 6.3 along side the dispersion of the unfiltered wavefront. All of the upstream traveling disturbances are removed and the disturbances at $\xi_x = 0$ m^{-1} are significantly reduced. Some of the stationary modes remain while only the acoustic and vibration signals that are propagating in the direction of flow remain. The aero-optical signal is clipped slightly at $\xi_x = 0$ due to the spatial width of the signal. The ratio of the time-averaged spatial-RMS of the filtered signal when compared to the aero-optic only signal was 1.24 while the unfiltered ratio was 1.53. When the filter was applied to only the aero-optic signal the ratio was 0.96. This filter method will retain any disturbance that is traveling in the direction of flow. Even with an ideal filter there is some slight attenuation of the aero-optical signal due to signal having some spectral width that crosses into upstream-moving portion of the dispersion plot.

6.3 Velocity Filtering

The dispersion plot shows flow structures that are traveling at a given speed as having a constant slope. A plane in the dispersion plot can be used to measure a flow structure's velocity in both x

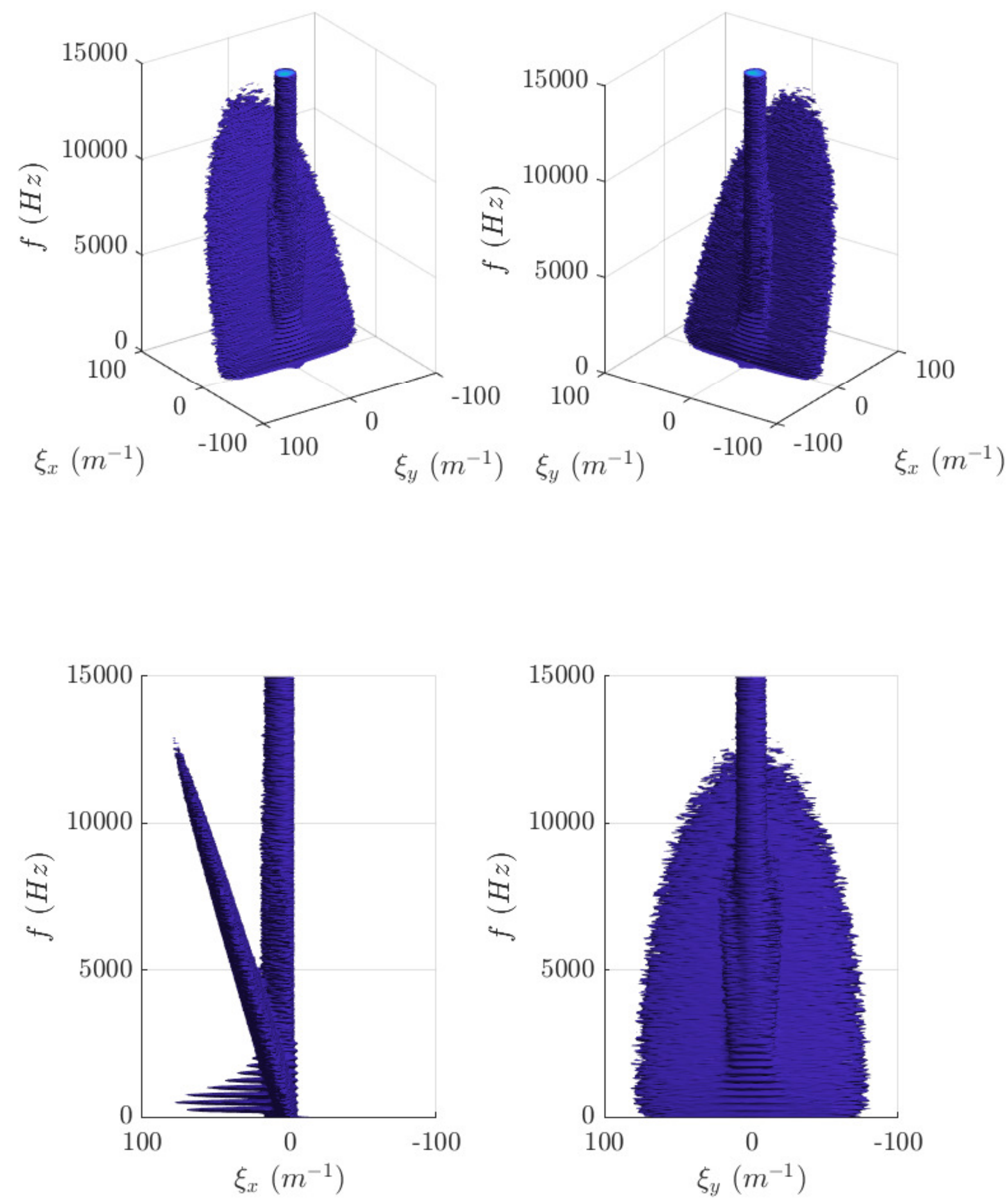

Figure 6.3. Dispersion isosurface of the synthetic wavefront with a downstream filter in place.

and y-directions. The distance from any given point in the dispersion plot to a plane described by the velocities v_x and v_y can be computed by

$$d = \frac{|v_x \xi_x + v_y \xi_y - f|}{\sqrt{v_x^2 + v_y^2 + 1}}. \tag{6.7}$$

A low-pass or high-pass filter can then be used to retain only disturbances that are traveling at that velocity, or to exclude those disturbances respectively.

A low-pass velocity-filter of the synthetic wavefront is shown in Figure 6.4. The filtered dispersion plot shows primarily only the aero-optic signal remains with some additional low-frequency content from the blade-passing frequency and harmonic disturbances as well as some stationary and acoustic disturbances. The ratio of the time-averaged spatial-RMS relative to that of the aero-optical only signal went from 1.53 in the unfiltered case to 1.01 in the filtered case. This method can provide a very effective way in quickly estimating the clean spatial-RMS of a contaminated wavefront.

Another use of the synthetic wavefront is measuring the speed of a broadband disturbance such as the aero-optical signal of a boundary layer. This is done by finding the velocity that maximizes the output spatial-RMS of the velocity filter, see Figure 6.5. In this case boundary layer speed was determined to be 163 m/s which corresponds to the design velocity of the synthetic signal of $0.8U$. If the velocity range used is to large, a false result can be obtained due to the inclusion of disturbance structures not related to the aero-optical signal. For signals that have a mean-velocity component that is not aligned with an axis both velocity components can be varied as shown in Figure 6.6. In this case a variable low-pass velocity filter was employed with a high-pass spatial filter operating in the radial direction. This helped eliminate some of the low-frequency stationary disturbances as well as some of the disturbances related to the blade-passing frequency. The velocity was measured using the optical disturbances in the dispersion plot to be approximately 207 m/s in the x-direction and -17 m/s in the y-direction.

6.4 Basic Filter Summary

Three different basic wavefront filters were shown and discussed in this chapter. The temporal filter is most useful when separating an optical wavefront into frequency bands. Adaptive optics system performance can be evaluated by using both high-pass and low-pass temporal filters. High-pass filters can be used to determine a systems performance that cannot be corrected while low-pass

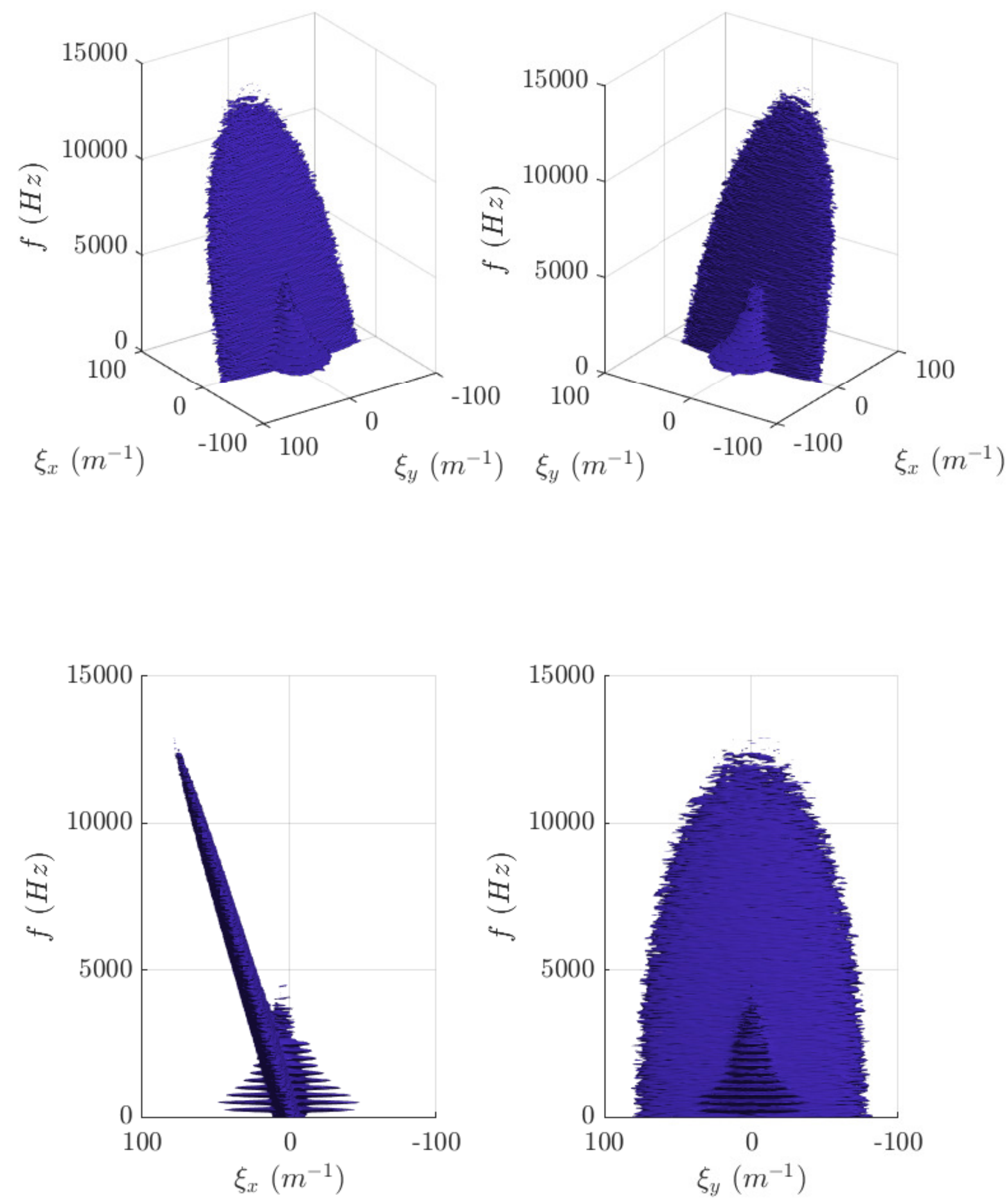

Figure 6.4. Dispersion isosurface of the synthetic wavefront with a low-pass velocity-filter in place.

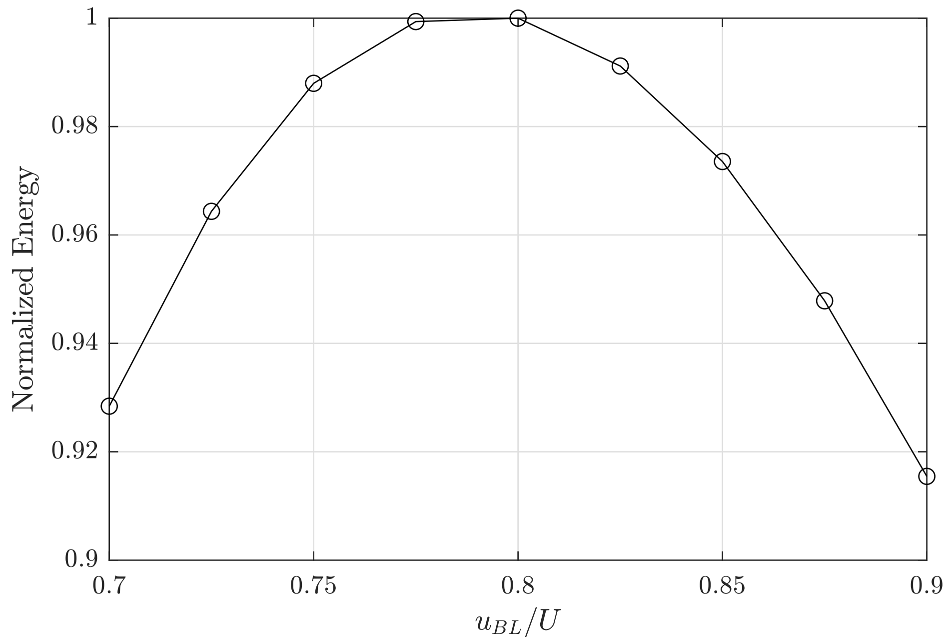

Figure 6.5. Velocity low-pass filter used to determine the mean disturbance velocity. The maximum value corresponds with the actual value used in the creation of the synthetic wavefront.

filters can be used to sizing the travel of active optical components. Band-pass filters are helpful in analyzing a wavefront over a narrow-band to examine the optical aberrations at specific frequencies that significantly contribute to the overall optical disturbance.

Filters that separate upstream and downstream-moving disturbances are useful as most of the optical contamination comes from acoustic signals that are traveling upstream form a wind-tunnel fan. These filters would also be useful for separating out an aero-optical signal that has a broad range of velocities that can occur in a span wise measurement of a boundary layer. Use some of sontag's data and site his dissertation.

The velocity filter is the most useful for isolating the aero-optical portion of a wavefront measurement given the aero-optical signal has a fairly narrow and constant velocity range. By using this filter to maximize the power over a range of velocities it can be used to measure the speed in both x and y-directions of an optical disturbance.

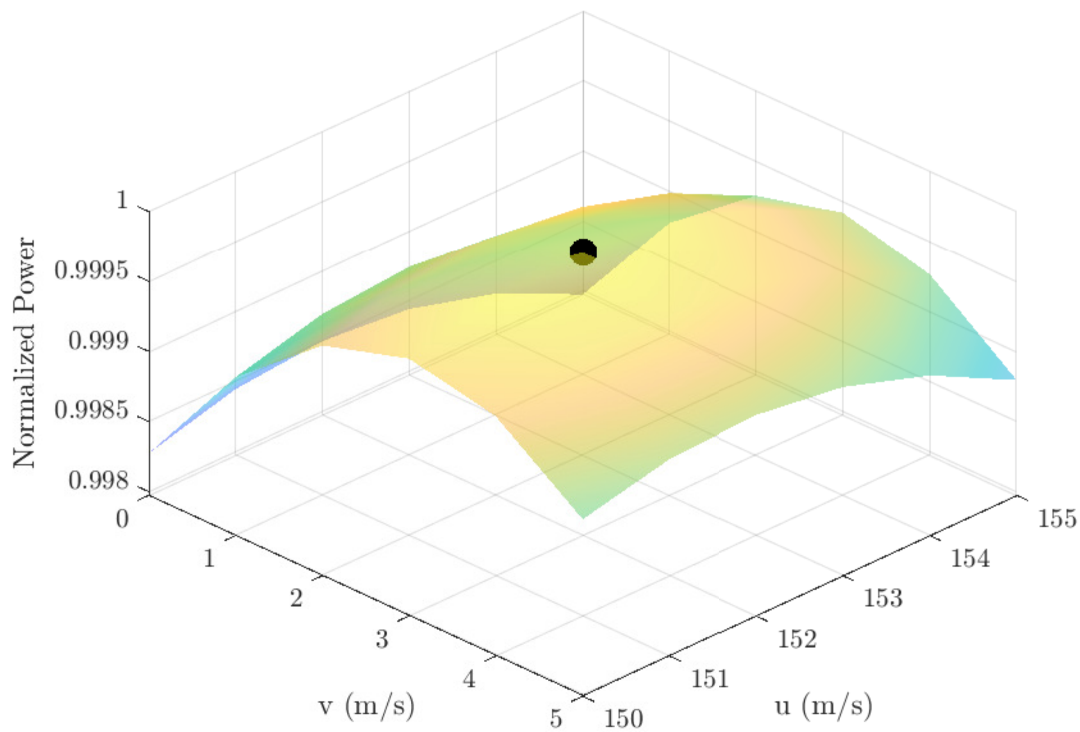

Figure 6.6. Velocity low-pass filter used to determine the mean disturbance velocity of measured data presented in Figure ??. The velocity in the x-direction was measured to be 207 m/s and -17 m/s in the y-direction.

CHAPTER 7

MULTIPLE SENSOR FILTERING TECHNIQUES

The previous chapter investigated filtering optical wavefront corruption by applying a variety of filters to the wavefront in the multi-dimensional spectral domain. These techniques involve only data from the optical wavefront itself and user knowledge and experience to obtain filtered data. When additional data streams are available, such as from microphones or accelerators, a targeted filter mechanisms become available.

A previous study [22] focused on using the combination of linear stochastic estimation (LSE) and spectral proper orthogonal decomposition (SPOD) to remove vibration related contamination from aero-optical wind-tunnel measurements. This process along with optical tip and tilt removal showed approximately an 85% reduction in the measured $\mathrm{OPD}_{\mathrm{RMS}}$ by combining accelerator measurements with optical wavefront measurements.

7.1 Optical Tip and Tilt

Zernike polynomials are traditionally used for describing optical aberrations of a optical system [3]. These polynomials are defined on the unit circle and form a set of orthogonal functions,

$$Z_n^m(\rho,\theta) = R_n^m(\rho)\cos(m\theta) \tag{7.1}$$

where $R_n^m(\rho)$ is the radial basis function and $\cos(m\theta)$ is the angular basis function. For values of $-m$ the angular basis function becomes $\sin(m\theta)$. The radial basis function are developed from Jacobi polynomials but for purposes in this study, only a few simple ones will be used. An optical wavefront can be approximated by a summation of Zernike polynomials multiplied by their corresponding coefficients

$$\mathrm{WF} \approx \sum Z_j a_j. \tag{7.2}$$

The Noll naming scheme is an method of organizing the Zernike polynomials into a single notation of Z_j, along with normalizing each polynomial to have a spatial RMS equal to one [27]. The first three of these using the Noll naming scheme are piston, tip, and tilt. Piston is simply the average OPD value of the single wavefront frame

$$Z_1 = 1. \tag{7.3}$$

Tip and tilt are the best planar fit to the OPD along the x-axis and y-axis respectively where tip is

$$Z_2 = 2\rho \cos\theta, \tag{7.4}$$

and tilt is

$$Z_3 = 2\rho \sin\theta. \tag{7.5}$$

Once the coefficients for these modes are solved for they can be filtered out

$$WF^F = WF - \sum Z_j a_j. \tag{7.6}$$

7.2 LSE-SPOD

The LSE-SPOD technique starts with performing SPOD on the primary data set and then using the Fourier transforms of the additional sensor data to perform a filtering operation. The spectral proper orthogonal decomposition technique is described in detail by Schmidt and Colonius [32]. A schematic of the SPOD algorithm is shown in Figure 7.1. The algorithm begins by separating the original data set, Q, into a number of smaller blocks,

$$Q = \begin{bmatrix} | & | & & | \\ q^{(1)} & q^{(2)} & \dots & q^{(N)} \\ | & | & & | \end{bmatrix}, \quad Q \in \mathbb{C}^{M\times N} \tag{7.7}$$

where M is the total number of degrees of freedom (number of spatial points times the block length in time) and N is the number of blocks. Each block is then Fourier Transformed in the temporal dimension or through all dimensions. Once in the frequency domain the data blocks are then reorganized by creating new blocks of identical temporal-frequencies,

$$\hat{Q} = \begin{bmatrix} | & | & & | \\ \hat{q}^{(1)} & \hat{q}^{(2)} & \dots & \hat{q}^{(N)} \\ | & | & & | \end{bmatrix}, \quad \hat{Q} \in \mathbb{C}^{M\times N} \tag{7.8}$$

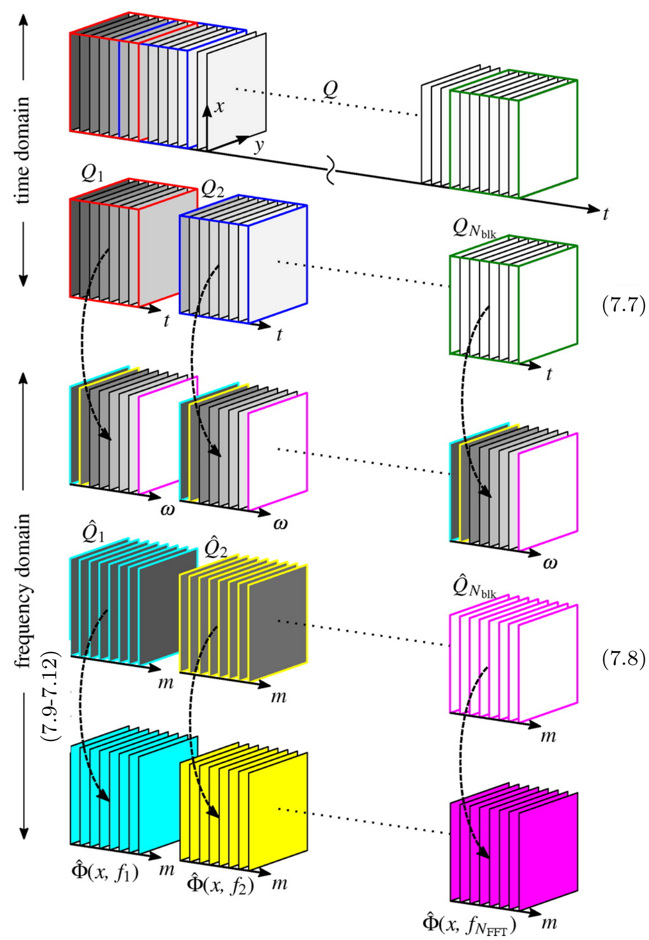

Figure 7.1. Schematic of the SPOD algorithm (taken from [32]). The numbers in parentheses denote the equations used.

where M is now the number of spatial points times the number of blocks and N is block length in time. Proper orthogonal decomposition is then performed separately on each temporal-frequency block via either traditional POD

$$\hat{C} = \frac{1}{N-1}\hat{Q}\hat{Q}^H, \tag{7.9}$$

$$\hat{C}W\hat{\Phi} = \hat{\Phi}\hat{\Lambda}, \tag{7.10}$$

or the method of snapshots,

$$\hat{Q}^H W \hat{Q}\hat{\Psi} = \hat{\Psi}\hat{\Lambda}, \tag{7.11}$$

$$\hat{\Phi} = \hat{Q}\hat{\Psi}, \tag{7.12}$$

where H denotes the Hermitian transpose, W is a weighting matrix, Φ is the set of deterministic spatial functions, Λ is the eigen-values, and Ψ is the coefficient matrix.

The linear stochastic estimation portion of the technique is described by Adrian [1]. This process uses a linear sum, L_{ij}, of additional measurements, y_j, to approximate a measured signal, x_i,

$$x_i^{LSE} = L_{ij}y_j, \tag{7.13}$$

where

$$L_{ij} = \langle x_i y_k \rangle \langle y_j y_k \rangle^{-1}. \tag{7.14}$$

When combined with SPOD, the estimation matrix, L, becomes

$$L = (\hat{\Psi}\hat{y}^H)(\hat{y}\hat{y}^H)^{-1}, \tag{7.15}$$

which allows for an estimated version of the coefficient matrix to be calculated

$$\hat{\Psi}^E = L\hat{y}. \tag{7.16}$$

The estimated coefficient matrix contains portions of the original signal that best resemble the additional sensor data. Assuming that the additional sensor data represents signal contamination of the original signal, a filtered coefficient matrix can be computed from the difference between the original and estimated coefficient matrix.

$$\hat{\Psi}^F = \hat{\Psi} - \hat{\Psi}^E. \tag{7.17}$$

A filtered signal, Q^F can be constructed by using the filtered coefficient matrix and the spatial functions,

$$\hat{Q} = \hat{\Psi}^F \hat{\Phi}^H. \tag{7.18}$$

7.3 Filtering Experimental Data

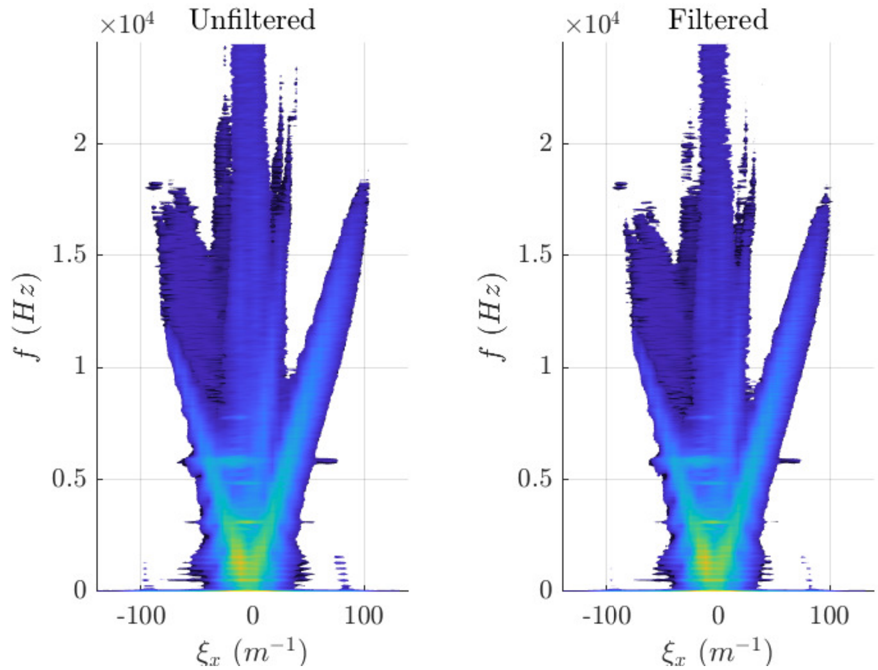

Figure 7.2. REPLACE

TABLE 7.1

REPLACE

	M=0.3	M=0.4	M=0.5
Original	0.0561	0.0521	0.0824
Tip/Tilt Removal	0.0120(78.6%)	0.0195(62.6%)	0.0291(64.7%)
Accelerometers	0.0102(81.8%)	0.0168(67.7%)	0.0251(69.5%)
Ambient Microphones	0.0103(81.7%)	0.0170(67.3%)	0.0254(69.1%)
Duct Microphones	0.0103(81.6%)	0.0170(67.3%)	0.0255(69.0%)
Test-Section Sensors	0.0103(81.6%)	0.0168(67.8%)	0.0252(69.4%)
All Sensors	0.0099(82.3%)	0.0163(68.8%)	0.0242(70.6%)
Velocity Filter	0.0090(83.9%)	0.0146(72.1%)	0.0217(73.7%)
+All Sensors	0.0075(86.7%)	0.0122(76.7%)	0.0181(78.0%)

APPENDIX A

SAMPLE CODE

Listing A.1: A simple function for computing the power spectra for vector `x` given an arbitrary windowing function.

```
function [sxx,freq] = simpleSXX(x,fsamp,window)
N = length(x);
x = reshape(x,1,N);
switch nargin
    case 1
        window = reshape(hann(N),1,N);
        fsamp = 1;
    case 2
        window = reshape(hann(N),1,N);
end
if isempty(fsamp)
    fsamp = 1;
end
if isa(window,'function_handle')
    window = reshape(window(N),1,N);
end
cw = 1/sqrt(sum(window.^2,'all')/N);
sxx = fftshift((abs(cw*fft(x.*window))).^2)/N/fsamp;
freq = (-0.5:1/N:0.5-1/N)*fsamp;
end
```

Listing A.2: A simple function for computing the dispersion or n-dimensional power spectra of `x` given an arbitrary windowing function.

```
function [sxx,frequency] = simpleSXXn(x,sampleRate,window)
% Check Number of Inputs - Select Default Options
switch nargin
    case 1
        window = 1;
        sampleRate = ones(1,ndims(x));
```

```
    case 2
        window = 1;
end
% Check if 'sampleRate' is Empty
if isempty(sampleRate)
    sampleRate = ones(1,ndims(x));
end
% Check if 'window' is a Function Handle
N = size(x);
if isa(window,'function_handle')
    wfun = window;
    window = wfun(N(1));
    for aa=2:ndims(x)
        window = window.*permute(wfun(N(aa)),aa:-1:1);
    end
end
% Calculate Window Correction
if window==1
    cw = 1;
else
    cw = 1/sqrt(sum(window.^2,'all')/numel(x));
end
% Calculate Power Spectra
sxx = fftshift((abs(cw*fftn(x.*window))).^2)/numel(x)/prod(sampleRate);
% Calculate Frequency Ranges
frequency{1} = (-0.5:1/N(1):0.5-1/N(1))'*sampleRate(1);
for aa=2:ndims(x)
    frequency{aa} = permute((-0.5:1/N(aa):0.5-1/N(aa))'*sampleRate(aa),aa:-1:1);
end
end
```

Listing A.3: MATLAB code used to generate the synthetic wavefront used in Chapter **??**.

```
close all; clc; clearvars; %#ok<*UNRCH>

sampleRate = [200*[1 1] 30000];
nSamples = 2.^[6 6 13];
c = 340;
M = 0.6;
uBL_u = 0.8;
surfaceStrength = -14.5;
```

```
nMakePlots = 0;      % 0: off, 1: plot, 2: plot and save, 3: Combo Only

% Frequency Space
freq.x = (-0.5:1/nSamples(2):0.5-1/nSamples(2))*sampleRate(2);
freq.y = reshape((-0.5:1/nSamples(1):0.5-1/nSamples(1))*sampleRate(1),nSamples(1),1,1);
freq.t = reshape((-0.5:1/nSamples(3):0.5-1/nSamples(3))*sampleRate(3),1,1,nSamples(3));
freq.rho = sqrt(freq.x.^2+freq.y.^2);
freq.theta = atan2(freq.y,freq.x);

%%%% Aero-Optics Signal
AO.ellipsoid = [8 90 175];
AO.strength = -14.5;
AO.slope = -0.13;
% Calculations
AO.speed = c*M*uBL_u;
b = 1/2/AO.strength*(AO.strength^2-1/AO.slope^2);
AO.WF = zeros(nSamples);
XR = freq.x*cos(atan(-1/AO.speed))+freq.t*sin(atan(-1/AO.speed));
YR = freq.y;
TR = -freq.t*sin(atan(-1/AO.speed))+freq.x*cos(atan(-1/AO.speed));
R = sqrt((XR/AO.ellipsoid(1)).^2+(YR/AO.ellipsoid(2)).^2+(TR/AO.ellipsoid(3)).^2);
AO.WF = 10.^(b-sqrt(R.^2/AO.slope^2+b^2));
clear b XR YR TR R;

%%%% White-Noise Stationary Signal
SN.rho0 = 5;
SN.strength = -14.5;
SN.slope = -0.175;
% Calculations
b = 1/2/SN.strength*(SN.strength^2-1/SN.slope^2);
SN.WF = 10.^(b-sqrt(repmat((freq.rho./(SN.rho0.*sqrt(10-6*cos(2*freq.theta+pi)))).^2,1,1,nSamples(3))/SN.slope^2+b^2));
clear b;

%%%% Blade Pass Frequency Contamination
BPF.freq = 500;
BPF.harmonic = 0.5:0.5:5;
BPF.rho0 = 20;
BPF.tThickness = 100;
```

```
BPF.strength = -14;
BPF.slope = -0.13;
BPF.cutoff = 500;
BPF.aspectRatio = 1;
% Calculations
b = 1/2/BPF.strength*(BPF.strength^2-1/BPF.slope^2);
BPF.WF = zeros(nSamples);
for aa=1:length(BPF.harmonic)
    R = sqrt((sqrt(freq.x.^2+(BPF.aspectRatio*freq.y).^2)./(BPF.rho0/sqrt(1+((BPF.freq*BPF.harmonic(aa)-BPF.freq)/BPF.cutoff).^2)*sqrt(10-6*cos(2*freq.theta+pi)))).^2+((freq.t-BPF.freq*BPF.harmonic(aa))/BPF.tThickness).^2);
    BPF.WF = BPF.WF+10.^(b-sqrt(R.^2/BPF.slope^2+b^2));
    R = sqrt((sqrt(freq.x.^2+(BPF.aspectRatio*freq.y).^2)./(BPF.rho0/sqrt(1+((BPF.freq*BPF.harmonic(aa)-BPF.freq)/BPF.cutoff).^2)*sqrt(10-6*cos(2*freq.theta+pi)))).^2+((freq.t+BPF.freq*BPF.harmonic(aa))/BPF.tThickness).^2);
    BPF.WF = BPF.WF+10.^(b-sqrt(R.^2/BPF.slope^2+b^2));
end
clear b R;

%%%% Zero Frequency Contamination
ZERO.rho0 = 25;
ZERO.tThickness = 50;
ZERO.strength = -14.5;
ZERO.slope = -0.5;
ZERO.aspectRatio = 0.55;
% Calculations
b = 1/2/ZERO.strength*(ZERO.strength^2-1/ZERO.slope^2);
R = sqrt((sqrt(freq.x.^2+(ZERO.aspectRatio*freq.y).^2)./(ZERO.rho0*sqrt(10-6*cos(2*freq.theta+pi)))).^2+(freq.t/ZERO.tThickness).^2);
ZERO.WF = 10.^(b-sqrt(R.^2/ZERO.slope^2+b^2));
clear b R;

%%%% Acoustic Cone Signal
CONE.strength = [-13 -16];
CONE.slope = -0.3;
CONE.thickness = 8;
CONE.lowPassRho = 200;
CONE.lowPassX = 115;
% Calculations
freqMod.x0 = sin(0.5*atan(1/c/(M+1))+0.5*atan(1/c/(M-1)))*freq.t;
freqMod.y0 = 0;
```

```
freqMod.ax = sin(0.5*atan(1/c/(M+1))-0.5*atan(1/c/(M-1)))*freq.t;
freqMod.ay = sin(atan(1/c))*freq.t;
freqMod.theta = atan2(freq.y-freqMod.y0,freq.x-freqMod.x0);
freqMod.rho = (sqrt((freq.x-freqMod.x0).^2+(freq.y-freqMod.y0).^2)./sqrt((freqMod.ax.*cos(freqMod.theta)).^2+(freqMod.ay.*sin(freqMod.theta)).^2)-1).*sqrt((freqMod.ax.*cos(freqMod.theta)).^2+(freqMod.ay.*sin(freqMod.theta)).^2)/CONE.thickness;
freqMod.rho(:,:,end/2+1) = freq.rho(:,:)/CONE.thickness;
b1 = ((CONE.strength(2)-CONE.strength(1))/(sampleRate(3)/2)*abs(freq.t)+CONE.strength(1));
b = 1/2./b1.*(b1.^2-1/CONE.slope^2);
CONE.WF = 10.^(b-sqrt(freqMod.rho.^2/CONE.slope^2+b.^2));
CONE.WF = CONE.WF.*sqrt(1./(1+(freqMod.rho/CONE.lowPassRho).^2));
CONE.WF = CONE.WF.*sqrt(1./(1+(freq.x/CONE.lowPassX).^2));
clear freqMod b b1;

%%%% Background Noise
BACK.strength = -18;
BACK.deviation = 0.75;
% Calculations
BACK.WF = 10.^(randn(nSamples)*BACK.deviation+BACK.strength);
BACK.WF(2:nSamples(1),2:nSamples(2),nSamples(3)/2+2:nSamples(3)) = flip(flip(flip(BACK.WF(2:nSamples(1),2:nSamples(2),2:nSamples(3)/2),1),2),3);

%%%% Sound and Vibration
SV.WF = BPF.WF+ZERO.WF+CONE.WF;

%%%% Plot
views = [-125 25; -55 25; 180 0; 270 0];
f1 = figure(1);
for aa=1:4
    subplot(2,2,aa)
    patch(isosurface(freq.x,freq.y,freq.t,AO.WF,10^surfaceStrength),'edgecolor','none','facecolor','red','facelighting','gouraud');
    patch(isosurface(freq.x,freq.y,freq.t,SN.WF,10^surfaceStrength),'edgecolor','none','facecolor','blue','facelighting','gouraud');
    patch(isosurface(freq.x,freq.y,freq.t,BPF.WF,10^surfaceStrength),'edgecolor','none','facecolor','green','facelighting','gouraud');
    patch(isosurface(freq.x,freq.y,freq.t,ZERO.WF,10^surfaceStrength),'edgecolor','none','facecolor','yellow','facelighting','gouraud');
    patch(isosurface(freq.x,freq.y,freq.t,CONE.WF,10^surfaceStrength),'edgecolor','none','facecolor','magenta','facelighting','gouraud');
```

```
    patch(isosurface(freq.x,freq.y,freq.t,BACK.WF,10^surfaceStrength),'edgecolor','none','facecolor','cyan','facelighting','gouraud');
    grid on;
    hold on;
    daspect([1 1 sampleRate(3)/sampleRate(1)/3]);
    xlim(sampleRate(1)/2*[-1 1]);
    ylim(sampleRate(2)/2*[-1 1]);
    zlim(sampleRate(3)/2*[0 1]);
    camlight;
    xlabel('$\xi_x\ (m^{-1})$','Interpreter','Latex');
    ylabel('$\xi_y\ (m^{-1})$','Interpreter','Latex');
    zlabel('$f\ (Hz)$','Interpreter','Latex');
%     title('Synthetic Signal','Interpreter','Latex');
    f1.Children(1).TickLabelInterpreter = 'latex';
    view(views(aa,:));
    camlight;
end
f1.Units = 'inches';
f1.Position = [1 1 6 8];
% Save Plot
saveas(f1,'synthetic_wavefront.eps','epsc');

%%%% Animation
nFrames = 150;
theta = (0:nFrames-1)/(nFrames)*4*pi;
az = rad2deg(theta);
el = 25*sin(theta/2);

f2 = figure(2);
scolor = parula(2);
patch(isosurface(freq.x,freq.y,freq.t(end/2+1:end),AO.WF(:,:,end/2+1:end),10^surfaceStrength),'edgecolor','none','facecolor','red','facelighting','gouraud');
patch(isocaps(freq.x,freq.y,freq.t(end/2+1:end),AO.WF(:,:,end/2+1:end),10^surfaceStrength,'all'),'edgecolor','none','facecolor','red','facelighting','gouraud');
patch(isosurface(freq.x,freq.y,freq.t(end/2+1:end),SN.WF(:,:,end/2+1:end),10^surfaceStrength),'edgecolor','none','facecolor','blue','facelighting','gouraud');
patch(isocaps(freq.x,freq.y,freq.t(end/2+1:end),SN.WF(:,:,end/2+1:end),10^surfaceStrength,'all'),'edgecolor','none','facecolor','blue','facelighting','gouraud');
```

```
patch(isosurface(freq.x,freq.y,freq.t(end/2+1:end),BPF.WF(:,:,end/2+1:end),10^surfaceStrength),'edgecolor','none','facecolor','green','facelighting','gouraud');
patch(isocaps(freq.x,freq.y,freq.t(end/2+1:end),BPF.WF(:,:,end/2+1:end),10^surfaceStrength,'all'),'edgecolor','none','facecolor','green','facelighting','gouraud');
patch(isosurface(freq.x,freq.y,freq.t(end/2+1:end),ZERO.WF(:,:,end/2+1:end),10^surfaceStrength),'edgecolor','none','facecolor','yellow','facelighting','gouraud');
patch(isocaps(freq.x,freq.y,freq.t(end/2+1:end),ZERO.WF(:,:,end/2+1:end),10^surfaceStrength,'all'),'edgecolor','none','facecolor','yellow','facelighting','gouraud');
patch(isosurface(freq.x,freq.y,freq.t(end/2+1:end),CONE.WF(:,:,end/2+1:end),10^surfaceStrength),'edgecolor','none','facecolor','magenta','facelighting','gouraud');
patch(isocaps(freq.x,freq.y,freq.t(end/2+1:end),CONE.WF(:,:,end/2+1:end),10^surfaceStrength,'all'),'edgecolor','none','facecolor','magenta','facelighting','gouraud');
patch(isosurface(freq.x,freq.y,freq.t(end/2+1:end),BACK.WF(:,:,end/2+1:end),10^surfaceStrength),'edgecolor','none','facecolor','cyan','facelighting','gouraud');
patch(isocaps(freq.x,freq.y,freq.t(end/2+1:end),BACK.WF(:,:,end/2+1:end),10^surfaceStrength,'all'),'edgecolor','none','facecolor','cyan','facelighting','gouraud');
grid on;
daspect([1 1 50]);
xlim(sampleRate(1)/2*[-1 1]);
ylim(sampleRate(2)/2*[-1 1]);
zlim(sampleRate(3)/2*[0 1]);
xlabel('$\xi_x\ (m^{-1})$','Interpreter','Latex');
ylabel('$\xi_y\ (m^{-1})$','Interpreter','Latex');
zlabel('$f\ (Hz)$','Interpreter','Latex');
f2.Children(1).TickLabelInterpreter = 'latex';
f2.Units = 'inches';
f2.Position = [1 1 5.5 6.25];
cl = camlight;

filename = 'synthetic_wavefront.gif';
frameRate = 15;
for aa=1:nFrames-1
    view(az(aa),el(aa));
```

```
    camlight(cl);
    drawnow;
    frame = getframe(f2);
    im = frame2im(frame);
    [imind,cm] = rgb2ind(im,256);
    if aa==1
        imwrite(imind,cm,filename,'gif','Loopcount',inf,'DelayTime',1/frameRate);
    else
        imwrite(imind,cm,filename,'gif','WriteMode','append','DelayTime',1/frameRate
            );
    end
end

%%%% Make Wavefronts
[wf.x,wf.y] = meshgrid(0.975*(-1:2/(nSamples(1)-1):1),0.975*(-1:2/(nSamples(2)-1):1)
    );
wf.rho = sqrt(wf.x.^2+wf.y.^2);
wf.theta = atan2(wf.y,wf.x);
wf.mask = ones(size(wf.x));
wf.mask(wf.rho>1) = NaN;
wf.x = wf.x.*wf.mask;
wf.y = wf.y.*wf.mask;
wf.rho = wf.rho.*wf.mask;
wf.theta = wf.theta.*wf.mask;
wf.sampleRate = sampleRate;
% Aero-Optics Signal
phase = pi*(2*rand(nSamples)-1);
phase(nSamples(1)/2+1,nSamples(2)/2+1,nSamples(3)/2+1) = 0;
phase(2:nSamples(1),2:nSamples(2),nSamples(3)/2+2:nSamples(3)) = -flip(flip(flip(
    phase(2:nSamples(1),2:nSamples(2),2:nSamples(3)/2),1),2),3);
wf.AO = real(ifftn(ifftshift(sqrt((AO.WF)*prod(sampleRate)*numel(AO.WF)).*exp(1i*
    phase))));
wf.AO = wf.AO.*wf.mask;
clear phase;
% White-Noise Stationary Signal
phase = pi*(2*rand(nSamples)-1);
phase(nSamples(1)/2+1,nSamples(2)/2+1,nSamples(3)/2+1) = 0;
phase(2:nSamples(1),2:nSamples(2),nSamples(3)/2+2:nSamples(3)) = -flip(flip(flip(
    phase(2:nSamples(1),2:nSamples(2),2:nSamples(3)/2),1),2),3);
wft.SN = real(ifftn(ifftshift(sqrt((SN.WF)*prod(sampleRate)*numel(SN.WF)).*exp(1i*
    phase))));
```

```
wft.SN = wft.SN.*wf.mask;
clear phase;
% Background Noise
phase = pi*(2*rand(nSamples)-1);
phase(nSamples(1)/2+1,nSamples(2)/2+1,nSamples(3)/2+1) = 0;
phase(2:nSamples(1),2:nSamples(2),nSamples(3)/2+2:nSamples(3)) = -flip(flip(flip(
    phase(2:nSamples(1),2:nSamples(2),2:nSamples(3)/2),1),2),3);
wft.BACK = real(ifftn(ifftshift(sqrt((BACK.WF)*prod(sampleRate)*numel(BACK.WF)).*exp
    (1i*phase))));
wft.BACK = wft.BACK.*wf.mask;
clear phase;
% Sound and Vibration
phase = pi*(2*rand(nSamples)-1);
phase(nSamples(1)/2+1,nSamples(2)/2+1,nSamples(3)/2+1) = 0;
phase(2:nSamples(1),2:nSamples(2),nSamples(3)/2+2:nSamples(3)) = -flip(flip(flip(
    phase(2:nSamples(1),2:nSamples(2),2:nSamples(3)/2),1),2),3);
wft.SV = real(ifftn(ifftshift(sqrt((SV.WF)*prod(sampleRate)*numel(SV.WF)).*exp(1i*
    phase))));
wft.SV = wft.SV.*wf.mask;
clear phase;
% Total
wf.wf = wf.AO+wft.SN+wft.BACK+wft.SV;
% Save
% save('synthetic_wavefront.mat','wf');
% disp('File Saved');
```

Listing A.4: MATLAB code used to filter wavefronts in Chapter **??**.

```
function [wf] = WFfilter(wf,varargin)
%WFFILTER Summary of this function goes here
%   Detailed explanation goes here

% Check Number of Inputs
if mod(nargin,2)==0 || nargin<3
    error('Invalid Number of Inputs');
end
% Zero-Out NaN Values
mask = double(~isnan(wf(:,:,1)));
mask(mask==0) = NaN;
% disp(mask);
wf(isnan(wf)) = 0;
```

```
% 3D-FFT
wf = fftshift(fftn(wf));
% Calculate Frequency
BlockSize = size(wf);
Frequency.y = reshape(-1/2:1/BlockSize(1):1/2-1/BlockSize(1),[],1);
Frequency.x = reshape(-1/2:1/BlockSize(2):1/2-1/BlockSize(2),1,[]);
Frequency.t = reshape(-1/2:1/BlockSize(3):1/2-1/BlockSize(3),1,1,[]);
Frequency.rho = sqrt(Frequency.x.^2+Frequency.y.^2);
% Filters
for aa=1:length(varargin)/2
    switch lower(varargin{2*aa-1})
        case 'time-highpass'
            if length(varargin{2*aa})==1
                n = 1;
            else
                n = varargin{2*aa}(2);
            end
            [b,a] = butter(n,varargin{2*aa}(1),'high','s');
            gain = abs(reshape(freqs(b,a,reshape(Frequency.t,1,[])),1,1,[]));
            clear b a;
        case 'time-lowpass'
            if length(varargin{2*aa})==1
                n = 1;
            else
                n = varargin{2*aa}(2);
            end
            [b,a] = butter(n,varargin{2*aa}(1),'low','s');
            gain = abs(reshape(freqs(b,a,reshape(Frequency.t,1,[])),1,1,[]));
            clear b a;
        case {'time-passband' 'time-bandpass'}
            if length(varargin{2*aa})==2
                n = 1;
            else
                n = varargin{2*aa}(3);
            end
            [b,a] = butter(n,varargin{2*aa}(1:2),'bandpass','s');
            gain = abs(reshape(freqs(b,a,reshape(Frequency.t,1,[])),1,1,[]));
            clear b a;
        case {'time-bandstop' 'time-stop'}
            if length(varargin{2*aa})==2
                n = 1;
```

```
            else
                n = varargin{2*aa}(3);
            end
            [b,a] = butter(n,varargin{2*aa}(1:2),'stop','s');
            gain = abs(reshape(freqs(b,a,reshape(Frequency.t,1,[])),1,1,[]));
            clear b a;
        case 'space-highpass'
            if length(varargin{2*aa})==1
                n = 1;
            else
                n = varargin{2*aa}(2);
            end
            gain = sqrt(1./(1+(Frequency.rho/varargin{2*aa}(1)).^(-2*n)));
        case 'space-lowpass'
            if length(varargin{2*aa})==1
                n = 1;
            else
                n = varargin{2*aa}(2);
            end
            gain = sqrt(1./(1+(Frequency.rho/varargin{2*aa}(1)).^(+2*n)));
        case 'velocity-highpass'
            if length(varargin{2*aa})==3
                n = 1;
            else
                n = varargin{2*aa}(4);
            end
            dist = abs(varargin{2*aa}(1)*Frequency.x+varargin{2*aa}(2)*Frequency.y-
                Frequency.t)/sqrt((varargin{2*aa}(1))^2+(varargin{2*aa}(2))^2+1);
            gain = sqrt(1./(1+(dist/varargin{2*aa}(3)).^(-2*n)));
        case 'velocity-lowpass'
            if length(varargin{2*aa})==3
                n = 1;
            else
                n = varargin{2*aa}(4);
            end
            dist = abs(varargin{2*aa}(1)*Frequency.x+varargin{2*aa}(2)*Frequency.y-
                Frequency.t)/sqrt((varargin{2*aa}(1))^2+(varargin{2*aa}(2))^2+1);
            gain = sqrt(1./(1+(dist/varargin{2*aa}(3)).^(+2*n)));
        case 'x-space'
            switch length(varargin{2*aa})==1
                case 1
```

```
                n = 1;
                threeDB = 0;
            case 2
                n = varargin{2*aa}(2);
                threeDB = 0;
            case 3
                n = varargin{2*aa}(2);
                threeDB = varargin{2*aa}(3);
        end
        if isempty(n)
            n = 1;
        end
        if threeDB
            gain = 1./(1+exp(-n*(Frequency.x-varargin{2*aa}(1)-log(sqrt(2)-1)/n)));
        else
            gain = 1./(1+exp(-n*(Frequency.x-varargin{2*aa}(1))));
        end
    case 'y-space'
        switch length(varargin{2*aa})==1
            case 1
                n = 1;
                threeDB = 0;
            case 2
                n = varargin{2*aa}(2);
                threeDB = 0;
            case 3
                n = varargin{2*aa}(2);
                threeDB = varargin{2*aa}(3);
        end
        if isempty(n)
            n = 1;
        end
        if threeDB
            gain = 1./(1+exp(-n*(Frequency.y-varargin{2*aa}(1)-log(sqrt(2)-1)/n)));
        else
            gain = 1./(1+exp(-n*(Frequency.y-varargin{2*aa}(1))));
        end
    case 'forward-moving'
        kx = BlockSize(2);
```

```
            kt = BlockSize(3);
            if ~isempty(varargin{2*aa})
                kx = kx*varargin{2*aa}(1);
                kt = kt*varargin{2*aa}(2);
            end
            gain = (2./(1+exp(-kx*Frequency.x))-1).*(2./(1+exp(-kt*Frequency.t))-1)/2+0.5;
        case 'backward-moving'
            kx = BlockSize(2);
            kt = BlockSize(3);
            if ~isempty(varargin{2*aa})
                kx = kx*varargin{2*aa}(1);
                kt = kt*varargin{2*aa}(2);
            end
            gain = (2./(1+exp(kx*Frequency.x))-1).*(2./(1+exp(-kt*Frequency.t))-1)/2+0.5;
        case 'forward-moving-ideal'
            gain = sign(Frequency.x.*Frequency.t)/2+0.5;
        case 'backward-moving-ideal'
            gain = -sign(Frequency.x.*Frequency.t)/2+0.5;
        case {'unity' 'no-filter'}
            gain = 1;
        otherwise
            warning('Invalid Filter Type.  Setting Gain to Unity.');
            gain = 1;
    end
%     disp(max(gain,[],'all'));
%     disp(min(gain,[],'all'));
    wf = wf.*gain;
    clear gain n;
end
% 3D-iFFT
wf = real(ifftn(ifftshift(wf))).*mask;
end
```

BIBLIOGRAPHY

1. R. J. Adrian. On the role of conditional averages in turbulence theory. In *Symposia on Turbulence in Liquids*, 1975.

2. R. B. Blackman and J. W. Tukey. *The Measurement of Power Spectra - From the Point of View of Communications Engineering*. Dover, 1958.

3. M. Born and E. Wolf. *Principles of Optics*. Pergamon, 1965.

4. Brüel & Kjær. 2670. https://www.bksv.com/-/media/literature/Product-Data/bp1584.ashx, November 2018. Product Data.

5. S. Butterworth. On the theory of filter amplifiers. *Experimental Wireless and the Wireless Engineer*, 7:536–541, 1930.

6. B. L. Catron, M. R. Rennie, S. Gordeyev, and E. J. Jumper. Effect of acoustic disturbances on aero-optical measurements. In *2018 Plasmadynamics and Lasers Conference*, 2018. doi: 10.2514/6.2018-3903.

7. B. L. Catron, M. R. Rennie, S. Gordeyev, and E. J. Jumper. Filtering of acoustic disturbances from aero-optical measurements. In *AIAA Scitech 2020 Forum*, 2020. doi: 10.2514/6.2020-0683.

8. A. CO. Sound measurement microphone. https://www.aco-japan.co.jp/pdf/en_microphone.pdf. Product Catalog.

9. N. De Lucca, S. Gordeyev, E. J. Jumper, and D. J. Wittich. Effects of engine acoustic waves on optical environment around turrets in-flight on aaol-t. *Optical Engineering*, 57(6), 2018. doi: 10.1117/1.OE.57.6.064107.

10. O. T. . E. Director. Fy99 annual report - airborne laser (abl). https://www.globalsecurity.org/military/library/budget/fy1999/dot-e/airforce/99abl.html, 2000.

11. E. J. Fitzgerald and E. J. Jumper. The optical distortion mechanism in a nearly incompressible free shear layer. *Journal of Fluid Mechanics*, 512:153–189, 2004. doi: 10.1017/S0022112004009553.

12. J. H. Gladstone and T. P. Dale. Researches on the refraction, dispersion, and sensitiveness of liquids. *Philosophical Transactions of the Royal Society of London*, 153:317–343, 1863.

13. J. W. Goodman. *Introduction to Fourier Optics*. McGraw-Hill, 1968.

14. S. Gordeyev, A. E. Smith, J. A. Cress, and E. J. Jumper. Experimental studies of aero-optical properties of subsonic turbulent boundary layers. *Journal of Fluid Mechanics*, 740:214–253, 2014. doi: 10.1017/jfm.2013.658.

15. F. Jacobsen and P. M. ller Juhl. *Fundamentals of General Linear Acoustics*. John Wiley & Sons, 2013.

16. W. C. G. Jr., Y. Hidaka, and T.Tanzawa. Refractivity of combustion gases. *Combustion and Flame*, 40:213–219, 1980. doi: 10.1016/0010-2180(81)90124-3.

17. E. J. Jumper and E. J. Fitzgerald. Recent advances in aero-optics. *Progress in Aerospace Sciences*, 37(3):299–339, 2001. doi: 10.1016/S0376-0421(01)00008-2.

18. E. J. Jumper, M. A. Zenk, S. Gordeyev, D. Cavalieri, and M. R. Whiteley. Airborne aero-optics laboratory. *Optical Engineering*, 52(7), 2013. doi: 10.1117/1.OE.52.7.071408.

19. M. V. Klein and T. E. Furtak. *Optics*. John Wiley & Sons, 2nd edition, 1986.

20. D. T. Kyrazis. Airborne laser laboratory departure from kirtland air force base and a brief history of aero-optics. *Optical Engineering*, 52(7), 2013. doi: 10.1117/1.OE.52.7.071403.

21. H. W. Liepmann. Deflection and diffusion of a light ray passing through a boundary layer. Technical Report SM-14397, Douglas Aircraft Company, Santa Monica Division, May 1952.

22. N. D. Lucca, S. Gordeyev, A. Smith, E. Jumper, M. Whiteley, and T. Neale. The removal of tunnel vibration induced corruption in aero-optical measurements. In *45th AIAA Plasmadynamics and Lasers Conference*, 2014. doi: 10.2514/6.2014-2494.

23. V. N. Mahajan. Strehl ratio for primary aberrations: some analytical results for circular and annular pupils. *Journal of the Optical Society of America*, 72(9):1258–1266, 1982. doi: 10.1364/JOSA.72.001258.

24. V. N. Mahajan. Strehl ratio for primary aberrations in terms of their aberration variance. *Journal of the Optical Society of America*, 73(6):860–861, 1983. doi: 10.1364/JOSA.73.000860.

25. P. M. Morse and K. U. Ingard. *Theoretical Acoustics*. McGraw-Hill, 1968.

26. M. L. Munjal. *Acoustics of Ducts and Mufflers*. John Wiley & Sons, 2nd edition, 2014.

27. R. J. Noll. Zernike polynomials and atmospheric turbulence. *Journal of the Optical Society of America*, 66(3):207–211, 1976. doi: 10.1364/JOSA.66.000207.

28. Peerless. XT25SC90-04. `https://tymphany-driver-files.s3.us-west-1.amazonaws.com/files/driver/pdfs/XT25SC90-04.Rev1.MP1%20-%20Product%20Sheet.pdf`, August 2021. Product Sheet - Revision: 1.

29. C. Porter, M. Rennie, and E. Jumper. Aero-optic effects of a wingtip vortex. *AIAA Journal*, 51(7):1533–1541, 2013. doi: 10.2514/1.J050899.

30. R. H. Randall. *An Introduction to Acoustics*. Dover Publications, 1951.

31. R. M. Rennie, D. A. Duffin, and E. J. Jumper. Characterization and aero-optic correction of a forced two-dimensional weakly compressible shear layer. *AIAA Journal*, 46(11):2787–2795, 2008. doi: 10.2514/1.35290.

32. O. T. Schmidt and T. Colonius. Guide to spectral proper orthogonal decomposition. *AIAA Journal*, 58(3):1023–1033, 2020. doi: 10.2514/1.J058809.

33. C. R. Service. Navy lasers, railgun, and gun-launched guided projectile: Background and issues for congress. `https://crsreports.congress.gov/product/pdf/R/R44175`, October 2021. Report R44175.

34. C. R. Service. Overview of department of defense use of the electromagnetic spectrum. `https://crsreports.congress.gov/product/pdf/R/R46564`, August 2021. Summary R46564.

35. C. R. Service. Defense primer: Directed-energy weapons. `https://crsreports.congress.gov/product/pdf/IF/IF11882`, July 2021. In Focus 11882.

36. J. P. Siegenthaler. *Guidelines for Adaptive-Optic Correction Based on Aperture Filtration*. Doctoral dissertation, University of Notre Dame, Notre Dame, IN, 2008.

37. J. P. Siegenthaler, S. Gordeyev, and E. Jumper. Shear layers and aperture effects for aero-optics. In *36th AIAA Plasmadynamics and Lasers Conference*, 2005. doi: 10.2514/6.2005-4772.

38. A. E. Smith, S. Gordeyev, and E. J. Jumper. Recent measurements of aero-optical effects caused by subsonic boundary layers. *Optical Engineering*, 52(7), 2013. doi: 10.1117/1.OE.52.7.071404.

39. H. A. Stine and W. Winovich. Light diffusion through high-speed turbulent boundary layers. Technical Report RM A56B21, National Advisory Committee For Aeronautics, May 1956.

40. S. L. Valley. Handbook of geophysiscs and space environments. Technical Report ADA056800, Air Force Cambridge Research Laboratories, April 1965.

41. K. Wang and M. Wang. Aero-optics of subsonic turbulent boundary layers. *Journal of Fluid Mechanics*, 696:122–151, 2012. doi: 10.1017/jfm.2012.11.